Journal of the Mechanics and Physics of Solids 110 (2018) 80–99

Contents lists available at ScienceDirect

Journal of the Mechanics and Physics of Solids

journal homepage: www.elsevier.com/locate/jmps

Crack nucleation in variational phase-field models of brittle fracture

E. Tanné[a,c], T. Li[b], B. Bourdin[c,*], J.-J. Marigo[a], C. Maurini[d]

[a] Laboratoire de Mécanique des solides, École Polytechnique, Route de Saclay, Palaiseau 91120, France
[b] IMSIA (UMR EDF-CNRS-CEA-ENSTA ParisTech 9219), Université Paris-Saclay, Palaiseau 91120, France
[c] Department of Mathematics and Center for Computation & Technology, Louisiana State University, Baton Rouge, LA 70803, USA
[d] Sorbonne Universités, UPMC Univ Paris 06, CNRS, UMR 7190, Institut Jean Le Rond d'Alembert, Paris F-75005, France

ARTICLE INFO

Article history:
Received 25 July 2017
Revised 10 September 2017
Accepted 11 September 2017
Available online 11 September 2017

Keywords:
Phase-field models of fracture
Crack nucleation
Size effects in brittle materials
Validation & verification
Gradient damage models
Smeared crack models

ABSTRACT

Phase-field models, sometimes referred to as gradient damage or smeared crack models, are widely used methods for the numerical simulation of crack propagation in brittle materials. Theoretical results and numerical evidences show that they can predict the propagation of a pre-existing crack according to Griffith' criterion. For a one-dimensional problem, it has been shown that they can predict nucleation upon a critical stress, provided that the regularization parameter be identified with the material's internal or characteristic length. In this article, we draw on numerical simulations to study crack nucleation in commonly encountered geometries for which closed-form solutions are not available. We use U- and V-notches to show that the nucleation load varies smoothly from that predicted by a strength criterion to that of a toughness criterion when the strength of the stress concentration or singularity varies. We present validation and verification numerical simulations for both types of geometries. We consider the problem of an elliptic cavity in an infinite or elongated domain to show that variational phase field models properly account for structural and material size effects.

Our main claim, supported by validation and verification in a broad range of materials and geometries, is that crack nucleation can be accurately predicted by minimization of a nonlinear energy in variational phase field models, and does not require the introduction of ad-hoc criteria.

1. Introduction

Despite its many successes, Griffith's theory of brittle fracture (Griffith, 1921) and its heir, Linear Elastic Fracture Mechanics (LEFM), still faces many challenges. In order to identify crack path, additional branching criteria whose choice is still unsettled have to be considered. Accounting for scale effects in LEFM is also challenging, as illustrated by the following example: consider a reference structure of unit size rescaled by a factor L. The critical loading at the onset of fracture scales then as $1/\sqrt{L}$, leading to a infinite nucleation load as the structure size approaches 0, which is inconsistent with experimental observation for small structures (Bažant, 1997; Issa et al., 2000; Chudnovsky, 2014).

* Corresponding author.
E-mail addresses: erwan.tanne@gmail.com (E. Tanné), tianyikillua@gmail.com (T. Li), bourdin@lsu.edu (B. Bourdin), marigo@lms.polytechnique.fr (J.-J. Marigo), corrado.maurini@upmc.fr (C. Maurini).

https://doi.org/10.1016/j.jmps.2017.09.006
0022-5096/

It is well accepted that this discrepancy is due to the lack of a critical stress (or a critical lengthscale) in Griffith's theory. Yet, augmenting LEFM to account for a critical stress is very challenging. In essence, the idea of material strength is incompatible with the concept of elastic energy release rate near stress singularity, the pillar of Griffith-like theories, as it would imply crack nucleation under an infinitesimal loading. Furthermore, a nucleation criterion based solely on pointwise maximum stress will be unable to handle crack formation in a body subject to a uniform stress distribution.

Many approaches have been proposed to provide models capable of addressing the aforementioned issues. Some propose to stray from Griffith fundamental hypotheses by incorporating cohesive fracture energies (Ortiz and Pandolfi, 1999; de Borst et al., 2004; Charlotte et al., 2006; Del Piero et al., 2013) or material non-linearities (Gou et al., 2015). Others have proposed dual-criteria involving both elastic energy release rate and material strength such as Leguillon (2002), for instance. Models based on the peridynamics theory (Silling, 2000) may present an alternative way to handle these issues, but to our knowledge, they are still falling short of providing robust quantitative predictions at the structural scale.

Francfort and Marigo (1998) set to devise a formulation of brittle fracture based *solely* on Griffith's idea of competition between elastic and fracture energy, yet capable of handling the issues of crack path and crack nucleation. However, as already pointed-out in Francfort and Marigo (1998), their model inherits a fundamental limitation of the Griffith theory and LEFM: the lack of an internal length scale and of maximum allowable stresses.

Amongst many numerical methods originally devised for the numerical implementation of the Francfort–Marigo model (Bourdin and Chambolle, 2000; Negri and Paolini, 2001; Fraternali, 2007; Schmidt et al., 2009), Ambrosio–Tortorelli regularizations (Ambrosio and Tortorelli, 1990; 1992), originally introduced in Bourdin et al. (2000), have become ubiquitous. They are nowadays known as phase-field models of fracture, and share several common points with the approaches coming from Ginzburg–Landau models for phase-transition (Karma et al., 2001). They have been applied to a wide variety of fracture problems including fracture of ferro-magnetic and piezo-electric materials (Abdollahi and Arias, 2012; Wilson et al., 2013), thermal and drying cracks (Maurini et al., 2013; Bourdin et al., 2014), or hydraulic fracturing (Bourdin et al., 2012; Wheeler et al., 2014; Chukwudozie, 2016; Wilson and Landis, 2016) to name a few. They have been expended to account for dynamic effects (Larsen et al., 2010; Bourdin et al., 2011; Borden et al., 2012; Hofacker and Miehe, 2013), ductile behavior (Alessi et al., 2014; Ambati et al., 2015a; Miehe et al., 2015), cohesive effects (Conti et al., 2016; Crismale and Lazzaroni, 2016; Freddi and Iurlano, 2017), large deformations (Ambati et al., 2015b; Borden et al., 2016; Miehe et al., 2016), or anisotropy (Li et al., 2014), for instance.

Although phase-field models were originally conceived as approximations of Francfort and Marigo's variational approach to fracture in the vanishing limit of their regularization parameter, a growing body of literature is concerned with their links with gradient damage models (Frémond and Nedjar, 1996; Lorentz and Andrieux, 2003). In this setting, the regularization parameter ℓ is kept fixed and interpreted as a material's internal length (Freddi and Royer Carfagni, 2010; Pham et al., 2011b; Del Piero, 2013). In particular, Pham and Marigo (2010a, 2010b) proposed an evolution principle for an Ambrosio–Tortorelli like energy based on irreversibility, stability and energy balance, where the regularization parameter ℓ is kept fixed and interpreted as a material's internal length. This approach, which we refer to as *variational phase-field* models, introduces a critical stress proportional to $1/\sqrt{\ell}$. As observed in Pham et al. (2011b); Bourdin et al. (2014); Nguyen et al. (2016), it can potentially reconcile stress and toughness criteria for crack nucleation, recover pertinent size effect at small and large length-scales, and provide a robust and relatively simple approach to model crack propagation in complex two- and three-dimensional settings. However, the few studies providing experimental verifications (Bourdin et al., 2014; Nguyen et al., 2016; Pham et al., 2017) are still insufficient to fully support this conjecture.

The goal of this article is precisely to provide such evidences, focusing on nucleation and size-effects for mode-I cracks. We provide quantitative comparison of nucleation loads near stress concentrations and singularities with published experimental results for a range of materials. We show that variational phase-field models can reconcile strength and toughness thresholds and account for scale effect at the structural and the material length-scale. In passing, we leverage the predictive power of our approach to propose a new way to measure a material's tensile strength from the nucleation load of a crack near a stress concentration or a weak singularity. In this study, we focus solely on the identification of the critical stress at the first crack nucleation event and are not concerned by the post-critical fracture behavior.

The article is organized as follows: in Section 2, we introduce variational phase-field models and recall some of their properties. Section 3 focuses on the links between stress singularities or concentrations and crack nucleation in these models. We provide validation and verification results for nucleation induced by stress singularities using V-shaped notches, and concentrations using U-notches. Section 4 is concerned with shape and size effects. We investigate the role of the internal length on nucleation near a defect, focusing on an elliptical cavity and a mode-I crack, and discussing scale effects at the material and structural length scales. Conclusions are finally drawn in Section 5.

2. Variational phase-field models

We start by recalling some important properties of variational phase-field models, focussing first on their construction as approximation method of Francfort and Marigo's variational approach to fracture, then on their alternative formulation and interpretation as gradient-damage models.

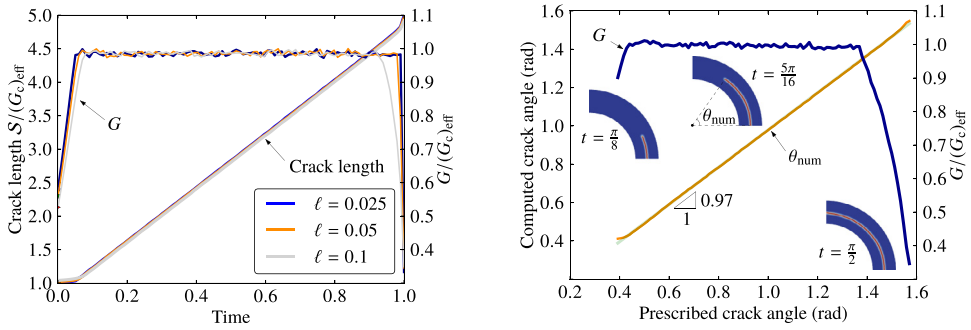

Fig. 1. Mode-I "surfing" experiment along straight (left) and circular (right) paths. Dependence of the crack length and elastic energy release rate on the loading parameter for multiple values of ℓ.

2.1. Regularization of the Francfort–Marigo fracture energy

Consider a perfectly brittle material with Hooke's law A and critical elastic energy release rate G_c occupying a region $\Omega \subset \mathbb{R}^n$, subject to a time dependent boundary displacement $\bar{u}$ on a part $\partial_D\Omega$ of its boundary and stress-free on the remainder $\partial_N\Omega$. In the variational approach to fracture, the quasi-static equilibrium displacement u_i and crack set Γ_i at a given discrete time step t_i are given by the minimization problem (see also Bourdin et al., 2008)

$$(u_i, \Gamma_i) = \underset{\substack{u=\bar{u}_i \text{ on } \partial_D\Omega \\ \Gamma \supset \Gamma_{i-1}}}{\operatorname{argmin}} \mathcal{E}(u,\Gamma) := \int_{\Omega\setminus\Gamma} \frac{1}{2} Ae(u)\cdot e(u)\,dx + G_c\mathcal{H}^{n-1}(\Gamma \cap \bar{\Omega} \setminus \partial_N\Omega), \tag{1}$$

where $\mathcal{H}^{n-1}(\Gamma)$ denotes the Hausdorff $(n-1)$–dimensional measure of the unknown crack Γ, *i.e.* its aggregate length in two dimensions or surface area in three dimensions, and $e(u) := \frac{1}{2}(\nabla u + \nabla^T u)$ denotes the symmetrized gradient of u.

Because in (1) the crack geometry Γ is unknown, special numerical methods had to be crafted. Various approaches based for instance on adaptive or discontinuous finite elements were introduced (Bourdin and Chambolle, 2000; Giacomini and Ponsiglione, 2003; Fraternali, 2007). Variational phase-field methods, take their roots in Ambrosio and Tortorelli's regularization of the Mumford–Shah problem in image processing (Ambrosio and Tortorelli, 1990; 1992), adapted to brittle fracture in Bourdin et al. (2000). In this framework, a regularized energy $\mathcal{E}_\ell$ depending on a regularization length $\ell > 0$ and a "phase–field" variable α taking its values in [0, 1] is introduced. A broad class of such functionals was introduced in Braides (1998). They are

$$\mathcal{E}_\ell(u,\alpha) = \int_\Omega \frac{a(\alpha)+\eta_\ell}{2} Ae(u)\cdot e(u)\,dx + \frac{G_c}{4c_w}\int_\Omega \left(\frac{w(\alpha)}{\ell} + \ell|\nabla\alpha|^2\right)dx, \tag{2}$$

where a and w are continuous monotonic functions such that $a(0) = 1$, $a(1) = 0$, $w(0) = 0$, and $w(1) = 1$, $\eta_\ell = o(\ell)$, and $c_w := \int_0^1 \sqrt{w(s)}\,ds$ is a normalization parameter. The approximation of $\mathcal{E}$ by $\mathcal{E}_\ell$ takes place with the framework of Γ–convergence (see Dal Maso, 1993; Braides, 2002 for instance). More precisely, if $\mathcal{E}_\ell$ Γ–converges to $\mathcal{E}$, then the global minimizers of $\mathcal{E}_\ell$ converge to that of $\mathcal{E}$. The Γ–convergence of a broad class of energies, including the ones above was achieved with various degrees of refinement going from static scalar elasticity to time discrete and time continuous quasi-static evolution linearized elasticity, and their finite element discretization (Bellettini and Coscia, 1994; Braides, 1998; Bourdin, 1999; Giacomini and Ponsiglione, 2003; Chambolle, 2004; 2005; Giacomini, 2005; Burke et al., 2010; 2013; Iurlano, 2014).

Throughout this article, we focus on two specific models:

$$\mathcal{E}_\ell(u,\alpha) = \int_\Omega \frac{(1-\alpha)^2+\eta_\ell}{2} Ae(u)\cdot e(u)\,dx + \frac{G_c}{2}\int_\Omega \left(\frac{\alpha^2}{\ell} + \ell|\nabla\alpha|^2\right)dx, \tag{AT$_2$}$$

introduced in Ambrosio and Tortorelli (1992) for the Mumford–Shah problem and in Bourdin et al. (2000) for brittle fracture, and

$$\mathcal{E}_\ell(u,\alpha) = \int_\Omega \frac{(1-\alpha)^2+\eta_\ell}{2} Ae(u)\cdot e(u)\,dx + \frac{3G_c}{8}\int_\Omega \left(\frac{\alpha}{\ell} + \ell|\nabla\alpha|^2\right)dx \tag{AT$_1$}$$

used in Bourdin et al. (2014).

The "surfing" problem introduced in Hossain et al. (2014) consists in applying a translating boundary displacement on $\partial\Omega$ given by $\bar{u}(x,y) = \bar{u}_I(x - Vt, y)$, where $\bar{u}_I$ denotes the asymptotic far-field displacement field associated with a mode-I crack along the x-axis with tip at (0, 0), V is a prescribed loading "velocity", and t a loading parameter ("time"). Fig. 1 (left) shows the outcome of a surfing experiment on a rectangular domain $\Omega = [0,5]\times[-\frac{1}{2},\frac{1}{2}]$ with an initial crack $\Gamma_0 = [0, l_0]\times\{0\}$ for several values of ℓ. The AT$_1$ model is used, assuming plane stress conditions, and the mesh size h is adjusted so that $\ell/h = 5$, keeping the "effective" numerical toughness $G_{\text{eff}} := G_c\left(1 + \frac{h}{4c_w\ell}\right)$ fixed (see Bourdin et al., 2008). The Poisson ratio

is $\nu = 0.3$, the Young's modulus is $E = 1$, the fracture toughness is $G_c = 1.5$, and the loading rate $V = 4$. As expected, after a transition stage, the crack length depends linearly on the loading parameter with slope 3.99; 4.00; 4.01 for $\ell = 0.1$; 0.05; 0.025 respectively. The elastic energy release rate G, computed using the G_θ method (Destuynder and Djaoua, 1981; Sicsic and Marigo, 2013; Li et al., 2016) is very close to G_{eff}. Even though Γ–convergence only mandates that the elastic energy release rate in the regularized energy converges to that of Griffith *as* $\ell \to 0$, we observe that as long as ℓ is "compatible" with the discretization size and domain geometry, its influence on crack propagation is insignificant. Similar observations were reported in Klinsmann et al. (2015), Pham et al. (2017), Zhang et al. (2017).

Fig. 1 (right) repeats the same experiment for a curve propagating along a circular path. Here, the boundary displacement is given by Muskhelishvili's exact solution for a crack propagating in mode-I along a circular path (Muskhelishvili, 1977). The Young's modulus, fracture toughness, and loading rate are set to 1. Again, we see that even for a *fixed* regularization length, the crack obeys Griffith's criterion.

When crack nucleation is involved, the picture is considerably different. Consider a one-dimensional domain of length L, fixed at one end and submitted to an applied displacement $\bar{u} = e\,L$ at the other end. For the lack of an elastic singularity, LEFM is incapable of predicting crack nucleation here, and predicts a structure capable of supporting arbitrarily large loads without failing. A quick calculation shows that the global minimizer of (1) corresponds to an uncracked elastic solution if $e < e_c := \sqrt{\frac{2G_c}{EL}}$, while at $e = e_c$, a single crack nucleates at an arbitrary location (see Francfort and Marigo, 1998; Bourdin et al., 2008). The failure stress is $\sigma_c = \sqrt{2G_cE/L}$, which is consistent with the scaling law $\sigma_c = \mathcal{O}\left(1/\sqrt{L}\right)$ mentioned in the introduction. The uncracked configuration is *always* a stable local minimizer of (1), so that if local minimization of (1) is considered, nucleation never takes place. Just as before, one can argue that for the lack of a critical stress, an evolution governed by the generalized Griffith energy (1) does not properly account for nucleation and scaling laws.

When performing global minimization of (2) using the backtracking algorithm of Bourdin (2007) for instance, a single crack nucleates at an ℓ–dependent load. As predicted by the Γ–convergence of $\mathcal{E}_\ell$ to $\mathcal{E}$, the critical stress at nucleation converges to $\sqrt{2G_cE/L}$ as $\ell \to 0$. Local minimization of (2) using the alternate minimizations algorithm of Bourdin et al. (2000), or presumably any gradient-based monotonically decreasing scheme, leads to the nucleation of a single crack at a critical load e_c, associated with a critical stress $\sigma_c = \mathcal{O}\left(\sqrt{G_cE/\ell}\right)$, as described in Bourdin (2007) for example. In the limit of vanishing ℓ, local and global minimization of (2) inherit therefore the weaknesses of Griffith-like theories when dealing with scaling properties and crack nucleation.

2.2. Variational phase-field models as gradient damage models

More recent works have seek to leverage the link between σ_c and ℓ. Ambrosio–Tortorelli functionals are then seen as the free energy of a gradient damage model (Frémond and Nedjar, 1996; Lorentz and Andrieux, 2003; Benallal and Marigo, 2007; Pham and Marigo, 2010a; 2010b) where α plays the role of a scalar *damage field*. In Pham et al. (2011b), a thorough investigation of a one-dimensional tension problem led to interpreting ℓ as a material's internal or characteristic length linked to a material's tensile strength. An overview of this latter approach, which is the one adopted in the rest of this work, is given below.

In all that follows, we focus on a *time-discrete* evolution but refer the reader to Pham and Marigo (2010a; 2010b); Marigo et al. (2016) for a time-continuous formulation which can be justified within the framework of generalized standard materials (Halphen and Nguyen, 1975) and rate-independent processes (Mielke, 2005). At any time step $i > 1$, the sets of admissible displacement and damage fields $\mathcal{C}_i$ and $\mathcal{D}_i$, equipped with their natural H^1 norm, are

$$\mathcal{C}_i = \{u \in H^1(\Omega) \,:\, u = \bar{u}_i \text{ on } \partial_D\Omega\},$$
$$\mathcal{D}_i = \{\beta \in H^1(\Omega) : \alpha_{i-1}(x) \le \beta(x) \le 1, \quad \forall x \in \Omega\},$$

where the constraint $\alpha_{i-1}(x) \le \beta(x) \le 1$ in the definition of $\mathcal{D}_i$ mandates that the damage be an increasing function of time, accounting for the irreversible nature of the damage process. The damage and displacement fields (u_i, α_i) are then local minimizers of the energy $\mathcal{E}_\ell$, *i.e.* there exists $h_i > 0$ such that

$$\forall (v,\beta) \in \mathcal{C}_i \times \mathcal{D}_i \text{ such that } \|(v,\beta) - (u_i,\alpha_i)\| \le h_i,\ \ \mathcal{E}_\ell(u_i,\alpha_i) \le \mathcal{E}_\ell(v,\beta), \tag{3}$$

where $\|\cdot\|$ denotes the natural H^1 norm of $\mathcal{C}_i \times \mathcal{D}_i$. We briefly summarize the solution of the uniaxial tension of a homogeneous bar (Pham et al., 2011a; 2011b), referring the reader to the recent review (Marigo et al., 2016) for further details: As one increases the applied strain, the damage field remains 0 and the stress field constant until it reaches the *elastic limit*

$$\sigma_e = \sqrt{\frac{G_cE}{c_w\ell}}\sqrt{\frac{w'(0)}{2s'(0)}}. \tag{4}$$

where E is the Young modulus of the undamaged material, and $s(\alpha) = 1/a(\alpha)$. If the applied displacement is increased further, the damage field increases but remains spatially constant. Stress hardening is observed until peak stress σ_c, followed by stress softening. A stability analysis shows that for long enough domains (*i.e.* when $L \gg \ell$), the homogeneous solution is never stable in the stress softening phase, and that a snap-back to a *fully localized solution* such that $\max_{x\in(0,L)} \alpha(x) = 1$ is observed. The profile of the localized solution and the width D of the localization can be derived explicitly from the

Table 1
Properties of the gradient damage models considered in this work: the elastic limit σ_e, the material strength σ_c, the width of the damage band D, and the conventional material length ℓ_{ch} defined in (5). We use the classical convention $E' = E$ in three dimension and in plane stress, and $E' = \frac{E}{1-\nu^2}$ in plane strain.

Model	$w(\alpha)$	$a(\alpha)$	c_w	σ_e	σ_c	D	ℓ_{ch}
$\mathtt{AT}_1$	α	$(1-\alpha)^2$	$\frac{2}{3}$	$\sqrt{\frac{3G_cE'}{8\ell}}$	$\sqrt{\frac{3G_cE'}{8\ell}}$	4ℓ	$\frac{8}{3}\ell$
$\mathtt{AT}_2$	α^2	$(1-\alpha)^2$	$\frac{1}{2}$	0	$\frac{3}{16}\sqrt{\frac{3G_cE'}{\ell}}$	∞	$\frac{256}{27}\ell$

functions a and w. With the choice of normalization of (2), the surface energy associated to the fully localized solution is exactly G_c and its elastic energy is 0, so that the overall response of the bar is that of a brittle material with toughness G_c and strength σ_c.

Knowing the material's toughness G_c and the Young's modulus E, one can then adjust ℓ in such a way that the peak stress σ_c matches the nominal material's strength. Let us denote by

$$\ell_{ch} = \frac{G_cE'}{\sigma_c^2} = \frac{K_{Ic}^2}{\sigma_c^2} \tag{5}$$

the classical material's *characteristic length* (see Rice, 1980; Falk et al., 2001, for instance), where $E' = E$ in three dimensions and in plane stress, or $E' = \frac{E}{1-\nu^2}$ in plane strain, and $K_{Ic} = \sqrt{G_cE'}$ is the mode-I critical stress intensity factor. The identification above gives

$$\ell_1 := \frac{3}{8}\ell_{ch}; \qquad \ell_2 := \frac{27}{256}\ell_{ch}, \tag{6}$$

for the $\mathtt{AT}_1$ and $\mathtt{AT}_2$ models, respectively.

Table 1 summarizes the specific properties of the $\mathtt{AT}_1$ and $\mathtt{AT}_2$ models. The $\mathtt{AT}_1$ model has some key conceptual and practical advantages over the $\mathtt{AT}_2$ model used in previous works, which were leveraged in Bourdin et al. (2014) for instance: it has a non-zero elastic limit, preventing diffuse damage at small loading. The length localization band D is finite so that equivalence with Griffith energy is obtained even for a finite value of ℓ, and not only in the limit of $\ell \to 0$, as predicted by Γ–convergence (Sicsic and Marigo, 2013). By remaining quadratic in the α and u variables, its numerical implementation using alternate minimizations originally introduced in Bourdin et al. (2000) is very efficient.

In all the numerical simulations presented below, the energy (2) is discretized using linear Lagrange finite elements, and minimization performed by alternating minimization with respect to u and α. Minimization with respect to u is a simple linear problem solved using preconditioned gradient conjugated while constrained minimization with respect to α is reformulated as a variational inequality and implemented using the variational inequality solvers provided by PETSc (Balay et al., 1997; 2016; 2017). All computations were performed using the open source implementations `mef90`[1] and `gradient-damage`.[2]

3. Effect of stress concentrations

The discussion above suggests that variational phase-field models, as presented in Section 2.2, can account for strength and toughness criteria simultaneously, on an idealized geometry. We propose to investigate this claim further by focusing on more general geometries, a V-shaped notch to illustrate nucleation near stress singularities and a U-shaped notch for stress concentrations. There is a wealth of experimental literature on crack initiation in such geometries using three-point bending (TPB), four-point bending (FPB), single or double edge notch tension (SENT and DENT) allowing us to provide qualitative validation and verification simulations of the critical load at nucleation.

3.1. Initiation near a weak stress singularity: the V-notch

Consider a V-shaped notch in a linear elastic isotropic homogeneous material. Let (r, θ) be the polar coordinate system emanating from the notch tip with $\theta = 0$ corresponding to the notch symmetry axis, shown on Fig. 2(left). Assuming that the notch lips $\Gamma^+ \cup \Gamma^-$ are stress-free, the mode-I component of the singular part of the stress field in plane strain is given

[1] Available at https://www.bitbucket.org/bourdin/mef90-sieve.
[2] Available at https://bitbucket.org/cmaurini/gradient-damage.

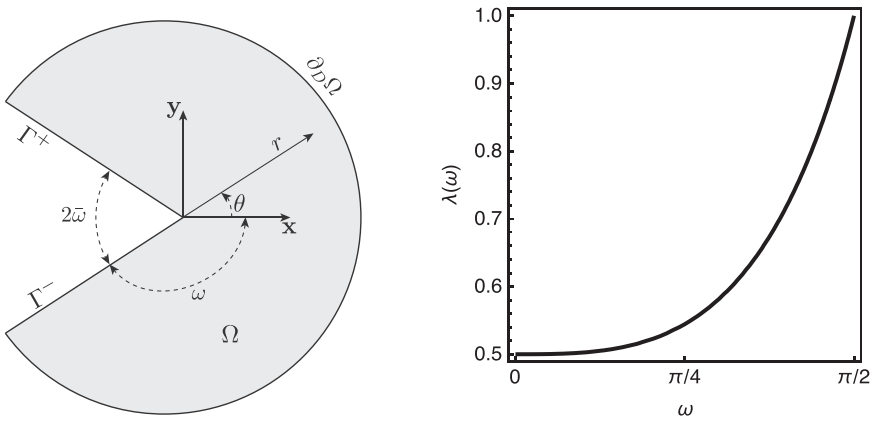

Fig. 2. Pac-man geometry for the study of the crack nucleation at a notch. Left: sketch of the domain and notation. Right: relation between the exponent of the singularity λ and the notch opening angle $\bar{\omega}$ determined by the solution of Eq. (10). For any opening angle $\bar{\omega}$ we apply on $\partial_D\Omega$ the displacement boundary condition obtained by evaluating on $\partial_D\Omega$ the asymptotic displacement (12) with $\lambda = \lambda(\omega)$.

in Leguillon and Sanchez-Palencia (1987):

$$\begin{aligned}\sigma_{\theta\theta} &= kr^{\lambda-1}F(\theta),\\ \sigma_{rr} &= kr^{\lambda-1}\frac{F''(\theta)+(\lambda+1)F(\theta)}{\lambda(\lambda+1)},\\ \sigma_{r\theta} &= -kr^{\lambda-1}\frac{F'(\theta)}{(\lambda+1)},\end{aligned} \tag{7}$$

where

$$F(\theta) = (2\pi)^{\lambda-1}\frac{\cos((1+\lambda)\theta) - f(\lambda,\bar{\omega})\cos((1-\lambda)\theta)}{1-f(\lambda,\bar{\omega})}, \tag{8}$$

and

$$f(\lambda,\bar{\omega}) = \frac{(1+\lambda)\sin((1+\lambda)(\pi-\bar{\omega}))}{(1-\lambda)\sin((1-\lambda)(\pi-\bar{\omega}))}, \tag{9}$$

and the exponent of the singularity $\lambda \in [1/2, 1]$, see Fig. 2(right), solves

$$\sin(2\lambda(\pi-\bar{\omega})) + \lambda\sin(2(\pi-\bar{\omega})) = 0. \tag{10}$$

From (7), it is natural to define a *generalized stress intensity factor*

$$k = \left.\frac{\sigma_{\theta\theta}}{(2\pi\, r)^{\lambda-1}}\right|_{\theta=0}. \tag{11}$$

Note that this definition differs from the one often encountered in the literature by a factor $(2\pi)^{\lambda-1}$, so that when $\omega = 0$ (*i.e.* when the notch degenerates into a crack), k corresponds to the mode-I stress intensity factor whereas when $\omega = \pi/2$, k is the tangential stress, and that the physical dimension of $[k] \equiv \mathrm{N/m}^{-\lambda-1}$ is not a constant but depends on the singularity power λ.

If $\bar{\omega} < \pi/2$ (*i.e.* $\omega > \pi/2$), the stress field is singular at the notch tip so that a nucleation criterion based on maximum pointwise stress will predict crack nucleation for any arbitrary small loading. Yet, as long as $\bar{\omega} > 0$ ($\omega < \pi$), the exponent of the singularity is sub-critical in the sense of Griffith, so that LEFM forbids crack nucleation, regardless of the magnitude of the loading.

3.1.1. The mode-I Pac-Man test

Consider a Pac-Man–shaped[3] domain with radius $L \gg \ell$ and notch angle $\bar{\omega}$ as in Fig. 2(left). In linear elasticity, a displacement field associated with the stress field (7) is

$$\begin{aligned}\bar{u}_r &= \frac{r^\lambda}{E}\frac{(1-\nu^2)F''(\theta)+(\lambda+1)[1-\nu\lambda-\nu^2(\lambda+1)]F(\theta)}{\lambda^2(\lambda+1)}\\ \bar{u}_\theta &= \frac{r^\lambda}{E}\frac{(1-\nu^2)F'''(\theta)+[2(1+\nu)\lambda^2+(\lambda+1)(1-\nu\lambda-\nu^2(\lambda+1)]F'(\theta)}{\lambda^2(1-\lambda^2)}.\end{aligned} \tag{12}$$

[3] https://en.wikipedia.org/wiki/Pac-Man.

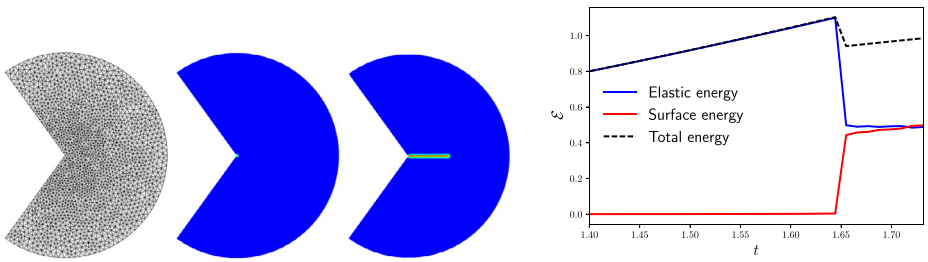

Fig. 3. Pac-Man test with the $\mathtt{AT}_1$ model, $L = 1$, $\ell = 0.015$, $\omega = 0.7\pi$, and $\nu = 0.3$. From left to right: typical mesh (with element size ten times larger than that in typical simulation for illustration purpose), damage field immediately before and after the nucleation of a crack, and plot of the energies versus the loading parameter t. Note the small damaged zone ahead of the notch tip before crack nucleation, and the energetic signature of a nucleation event.

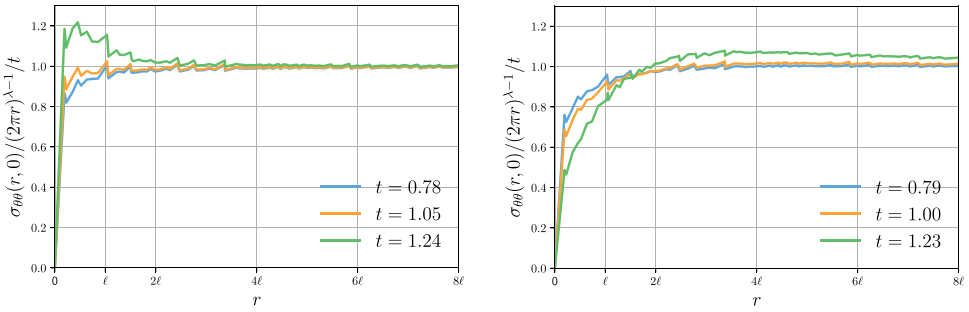

Fig. 4. Identification of the generalized stress intensity factor: $\frac{\sigma_{\theta\theta}(r,0)}{(2\pi r)^{\lambda-1}}$ along the domain symmetry axis for the $\mathtt{AT}_1$(left) and $\mathtt{AT}_2$(right) models with undamaged notch conditions, and sub-critical loadings. The notch aperture is $\bar{\omega} = \pi/10$.

In the mode-I Pac-Man test, we apply a boundary displacement on the outer edge of the domain $\partial_D\Omega$ of the form $t\bar{u}$ on both components of u, t being a monotonically increasing loading parameter.

We performed series of numerical simulations varying the notch angle $\bar{\omega}$ and regularization parameter ℓ for the $\mathtt{AT}_1$ and $\mathtt{AT}_2$ models. Up to a rescaling and without loss of generality, it is always possible to assume that $E = 1$ and $G_c = 1$. The Poisson ratio was set to $\nu = 0.3$. We either prescribed the value of the damage field on $\Gamma^+ \cup \Gamma^-$ to 1 (we refer this to as "damaged notch conditions") or let it free ("undamaged notch conditions"). The mesh size was kept at a fixed ratio of the internal length $h = \ell/5$.

For "small" enough loadings, we observe an elastic or nearly elastic phase during which the damage field remains 0 or near 0 away from an area of radius $o(\ell)$ near the notch tip. Then, for some loading $t = t_c$, we observed the initiation of a "large" add-crack associated with a sudden jump of the elastic and surface energy. Fig. 3 shows a typical mesh, the damage field immediately before and after nucleation of a macroscopic crack and the energetic signature of the nucleation event.

Fig. 4 shows that up to the critical loading, the generalized stress intensity factor can be accurately recovered by averaging $\sigma_{\theta\theta}(r,0)/(2\pi\, r)^{\lambda-1}$ along the symmetry axis of the domain, provided that the region $r \leq 2\ell$ be excluded.

Fig. 5(left) shows the influence of the internal length on the critical generalized stress intensity factor for a sharp notch ($\bar{\omega} = 0.18^\circ$) for the $\mathtt{AT}_1$ and $\mathtt{AT}_2$ models, using damaged and undamaged notch boundary conditions on the damage field. In this case, with the normalization (11), the generalized stress intensity factor coincides with the standard mode-I stress intensity factor K_{Ic}. As suggested by the surfing experiment in the introduction, the internal length ℓ also has a very minor influence on the critical load $t := k_c^{AT} \simeq K_{Ic} = \sqrt{G_c E'}$. As reported previously in Klinsmann et al. (2015) for instance, undamaged notch conditions lead to overestimating the critical load. We speculate that this is because with undamaged notch condition, the energy barrier associated with bifurcation from an undamaged (or partially damaged) state to a fully localized state needs to be overcome. As expected, this energy barrier is larger for the $\mathtt{AT}_1$ model than for the $\mathtt{AT}_2$ model for which large damaged areas ahead of the notch tip are observed.

For flat notches ($2\bar{\omega} = 179.64^\circ$) as shown in Fig. 5(right), the generalized stress intensity factor k takes the dimension of a stress, and crack nucleation is observed when k_c reaches the ℓ–dependent value σ_c given in Table 1, *i.e.* when $\sigma_{\theta\theta}|_{\theta=0} = \sigma_c$, as in the uniaxial tension problem. In this case the type of damage boundary condition on the notch seems to have little influence.

For intermediate values of $\bar{\omega}$, we observe in Fig. 6 that the critical generalized stress intensity factor varies smoothly and monotonically between its extreme values and remains very close to K_{Ic} for opening angles as high as 30°, which justifies the common numerical practice of replacing initial cracks with slightly open sharp notches and damaged notch boundary conditions. See Table A.3 for numerical data.

Table 2
Material properties used in the numerical simulations as given in the literature.

Material	E [MPa]	ν	K_{Ic} [MPa $\sqrt{\text{m}}$]	σ_c [MPa]	Source
Al_2O_3–7%ZrO_2	350,000	0.24	4.1	290	Yosibash et al. (2004)
PMMA	2300	0.36	1.03	124	Dunn et al. (1997); Yosibash et al. (2004)
Plexiglass	3000	0.36	1.86	104.9	Seweryn (1994)
PVC H80	85	0.32	0.32	2.51	Gómez and Elices (2003); Grenestedt et al. (1996)
PVC H100	125	0.32	0.26	4.02	Gómez and Elices (2003); Grenestedt et al. (1996)
PVC H130	175	0.32	0.34	5.70	Gómez and Elices (2003); Grenestedt et al. (1996)
PVC H200	310	0.32	0.57	9.38	Gómez and Elices (2003); Grenestedt et al. (1996)
Steel	205,000	0.3	52	1170	Gómez and Elices (2003); Strandberg (2002)
Duraluminium	70,000	0.3	50.6	705	Seweryn (1994)

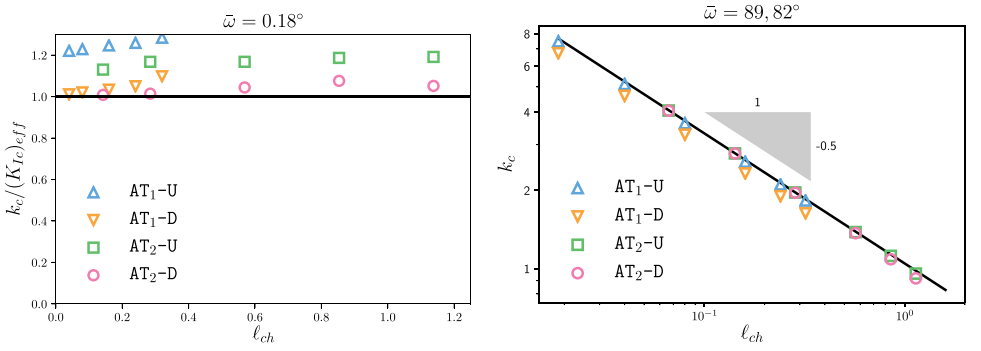

Fig. 5. Critical generalized critical stress intensity factor at crack nucleation as a function of the internal length for $\bar{\omega} \simeq 0$ (left) and $\omega \simeq \pi/2$ (right). $\texttt{AT}_1$–U, $\texttt{AT}_1$–D, $\texttt{AT}_2$–U, and $\texttt{AT}_2$–D refer respectively to computations using the $\texttt{AT}_1$ model with damaged notch and undamaged notch boundary conditions, and the $\texttt{AT}_2$ model with damaged notch and undamaged notch boundary conditions. $(K_{Ic})_{\text{eff}} := \sqrt{\frac{G_{\text{eff}}E}{1-\nu^2}}$ denotes the critical mode-I stress intensity factor modified to account for the effective toughness G_{eff}.

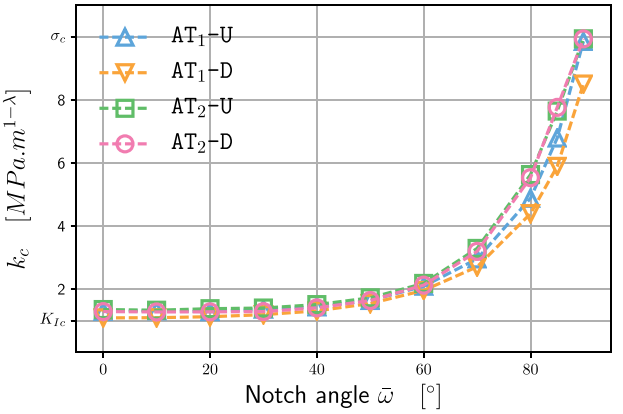

Fig. 6. Critical generalized stress intensity factor k for crack nucleation at a notch as a function of the notch opening angle $\bar{\omega}$. Results for the $\texttt{AT}_1$ and $\texttt{AT}_2$ models with damaged -D and undamaged -U notch lips conditions. The results are obtained with numerical simulations on the Pac-Man geometry with $(K_{Ic})_{\text{eff}} = 1$ and $\ell = 0.01$ so that $\sigma_c = 10$ under plane-strain conditions with a unit Young's modulus and a Poisson ratio $\nu = 0.3$.

3.1.2. Validation

For intermediate values $0 < 2\bar{\omega} < \pi$, we focus on validation against experiments from the literature based on measurements of the generalized stress intensity factor at a V-shaped notch.

Data from single edge notch tension (SENT) test of soft annealed tool steel, (AISI O1 at –50°C (Strandberg, 2002), four point bending (FPB) experiments of Divinycell ® H80, H100, H130, and H200 PVC foams) (Grenestedt et al., 1996), and double edge notch tension (DENT) experiments of poly methyl methacrylate (PMMA) and Duraluminium (Seweryn, 1994), were compiled in Gómez and Elices (2003). We performed a series of numerical simulations of Pac-Man tests using the material properties reported in Gómez and Elices (2003) and listed in Table 2. In all cases, the internal length ℓ was computed using (6).

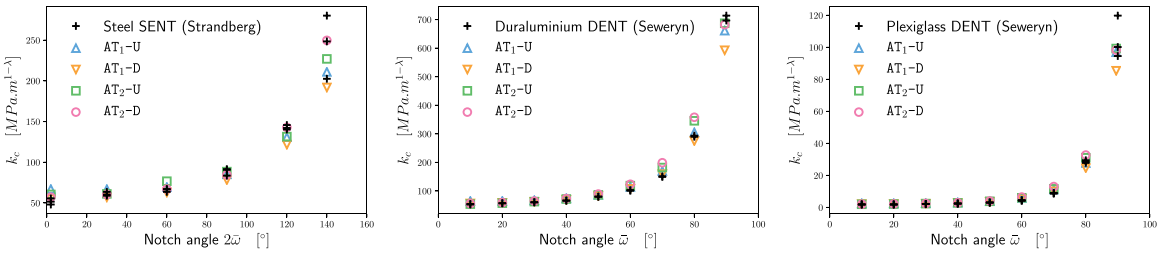

Fig. 7. Critical generalized stress intensity factor k_c vs notch angle. Comparison between numerical simulations with the $\mathtt{AT}_1$ and $\mathtt{AT}_2$ models and damaged and undamaged boundary conditions on the notch edges with experiments in steel from Strandberg (2002) (left), and Duraluminium (middle) and PMMA (right) from Seweryn (1994).

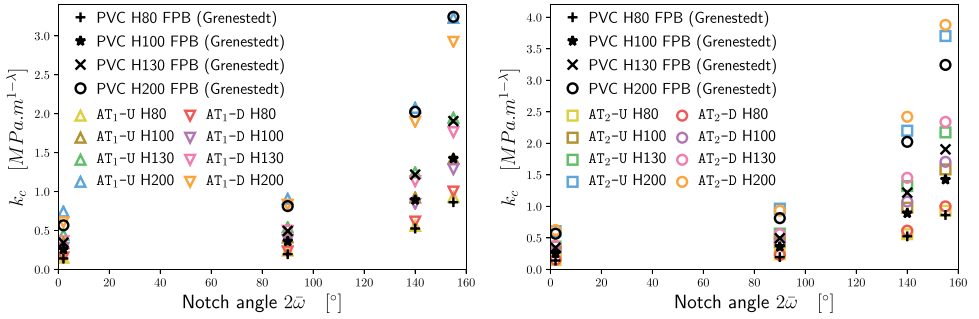

Fig. 8. Critical generalized stress intensity factor k_c vs notch angle and depth in PVC foam samples from Grenestedt et al. (1996). Numerical simulations with the $\mathtt{AT}_1$ model with damaged and undamaged notch conditions (left), and $\mathtt{AT}_2$ model with damaged and undamaged notch conditions (right).

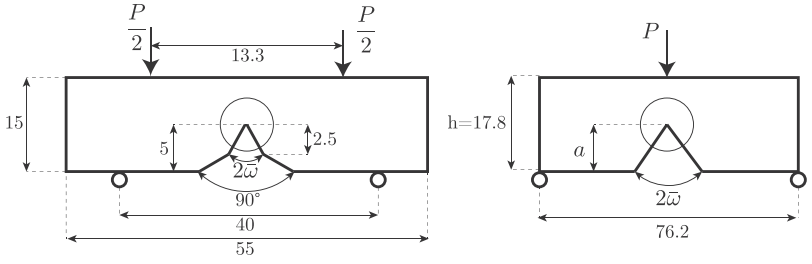

Fig. 9. Schematic of the geometry and loading in the four point bending experiments of Yosibash et al. (2004) (left) and three point bending experiments of Dunn et al. (1997) (right). The geometry of the three point bending experiment of Yosibash et al. (2004) is identical to that of their four point bending, up to the location of the loading devices.

Figs. 7 and 8 compare the critical generalized stress intensity factor from our numerical simulations with experimental values reported in the literature for V-notch with varying aperture. The definition (11) for k is used. For the $\mathtt{AT}_1$ model, we observe a good agreement for the entire range of notch openings, as long as damaged notch conditions are used for small notch angles and undamaged notch conditions for large notch angles. For the $\mathtt{AT}_2$ model, the same is true, but the agreement is not as good for large notch angles, due to the presence of large areas of distributed damage prior to crack nucleation.

The numerical values of the critical generalized stress intensity factors for the $\mathtt{AT}_1$ models and the experiments from the literature are included in Tables A.4, A.5, A.6, and A.7 using the convention of (11) for k. As suggested by Fig. 5 and reported in the literature (see Klinsmann et al., 2015), nucleation is best captured if damaged notch boundary conditions are used for sharp notches and undamaged notch conditions for flat ones.

These examples strongly suggest that variational phase-field models of fracture are capable of predicting mode-I nucleation in stress and toughness dominated situations, as seen above, but also in the intermediate cases. Conceptually, toughness and strength (or equivalently internal length) could be measured by matching generalized stress intensity factors in experiments and simulations. When doing so, however, extreme care has to be exerted in order to ensure that the structural geometry has no impact on the measured generalized stress. Similar experiments were performed in Dunn et al. (1997); Yosibash et al. (2004) for three and four point bending experiments on PMMA and aluminum oxide–zirconia ceramics samples. While the authors kept the notch angle fixed, they performed three and four point bending experiments or varied the relative depth of the notch as a fraction of the sample height (see Fig. 9).

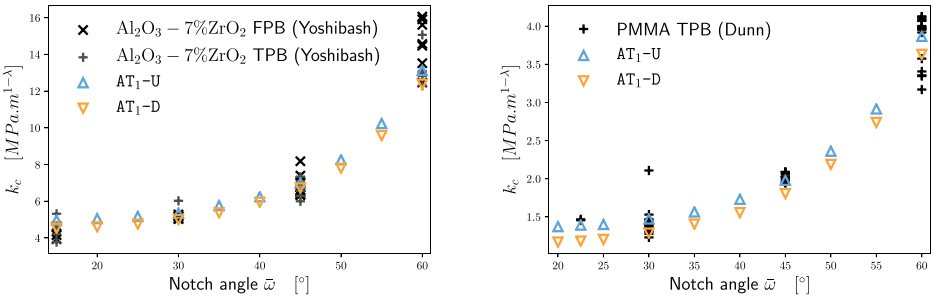

Fig. 10. Critical generalized stress intensity factor k_c vs notch angle for $Al_2O_3-7\%ZrO_2$(left) and PMMA (right). The black markers represents all experimental results. The numerical results are obtained through the Pac-Man test using the AT_1 model. See Tables A.8 and A.9 in the Appendix for the raw data.

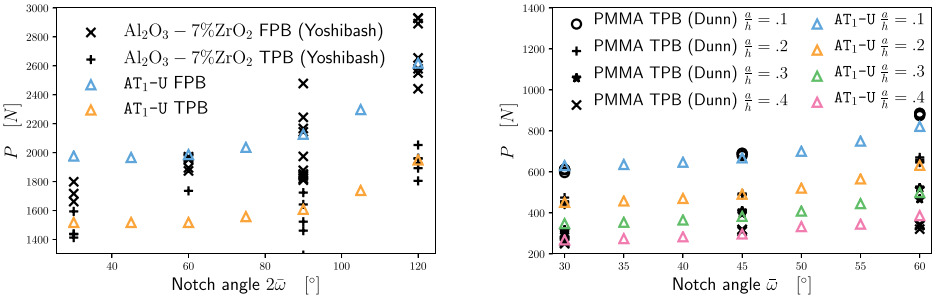

Fig. 11. Critical load in the three- and four-point bending experiments of a Al_2O_3–$7\%ZrO_2$ sample (left) and four-point bending of a PMMA sample (right) from Yosibash et al. (2004) compared with numerical simulations using the AT_1 model and undamaged notch boundary conditions. Due to significant variations in measurements in the first set of experiments, each data point reported in Yosibash et al. (2004) is plotted. For the PMMA experiments, average values are plotted. See Table A.10 and A.11 in the Appendix for raw data.

Fig. 10 compares numerical values of the generalized stress intensity factor using the AT_1 model with experimental measurements, and the actual numerical values are included in Table A.8 and A.9.

For the aluminum oxide–zirconia ceramic, we observe that the absolute error between measurement and numerical prediction is typically well within the standard deviation of the experimental measurement. As expected, damaged notch boundary conditions lead to better approximation of k_c for small angles, and undamaged notches are better for larger values of $\bar{\omega}$.

For the three point bending experiments in PMMA of Dunn et al. (1997) later reported in Yosibash et al. (2004), the experimental results suggest that the relative depth a/h of the notch has a significant impact on k_c. We therefore performed full-domain numerical simulation using the geometry and loading from the literature, and compared the critical force upon which a crack nucleates in experiments and simulations. All computations were performed using the AT_1 model in plane strain with undamaged notch boundary conditions. Fig. 11 compares the experimental and simulated value of the critical load at failure, listed in Table A.10 and A.11.

These simulations show that a robust quantitative prediction of the failure load in geometries involving a broad range of stress singularity power can be achieved numerically with the AT_1 model, provided that the internal length be computed using (6), which involves only *material properties*. In other words, our approach is capable of predicting crack nucleation near a weak stress singularity using only elastic properties, fracture toughness G_c, the tensile strength σ_c, and the local energy minimization principle (3).

In light of Fig. 11, we suggest that both toughness and tensile strength (or equivalently toughness and internal length) can be measured by matching full domain or Pac-Man computations and experiments involving weak elastic singularity of various power (TPB, FPB, SENT, DENT with varying notch depth or angle) instead of measuring σ_c directly. We expect that this approach will be much less sensitive to imperfections than the direct measurement of tensile strength, which is virtually impossible. Furthermore, since our criterion is not based on crack tip asymptotics, using full domain computations do not require that the experiments be specially designed to isolated the notch tip singularity from structural scale deformations.

3.2. Initiation near a stress concentration: the U-notch

Crack nucleation in a U-shaped notch is another classical problem that has attracted a wealth of experimental and theoretical work. Consider a U-shaped notch of width ρ and length $a \gg \rho$ subject to a mode-I local loading (see Fig. 12 for a description of notch geometry in the context of a double edge notch tension sample). Assuming “smooth” loadings and applied boundary displacements, elliptic regularity mandates that the stress field be non-singular near the notch tip, provided

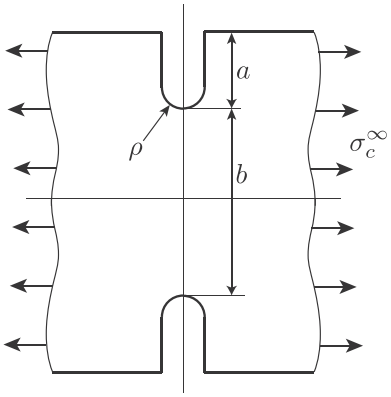

Fig. 12. DENT geometry.

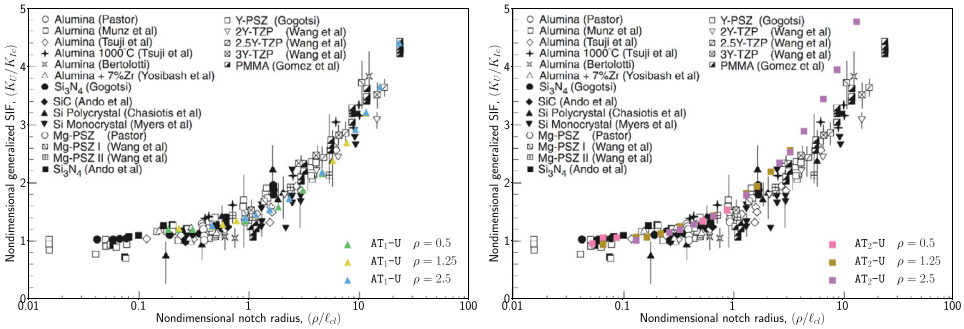

Fig. 13. Crack nucleation at U-notches. Comparison between experimental data of Gómez et al. (2006) and numerical simulations using the $\mathtt{AT}_1$ (left) and $\mathtt{AT}_2$ (right) models.

that $\rho > 0$. Within the realm of Griffith fracture, this of course makes crack nucleation impossible. As it is the case for the V-notch, introducing a nucleation principle based on a critical stress is also not satisfying as it will lead to a nucleation load going to 0 as $\rho \to 0$, instead of converging to that of an infinitely thin crack given by Griffith's criterion. There is a significant body of literature on "notch mechanics", seeking to address this problem introducing stress based criteria, generalized stress intensity factors, or intrinsic material length and cohesive zones. A survey of such models, compared with experiments on a wide range of brittle materials is given (Gómez et al., 2006).

In what follows, we study crack nucleation near *stress concentrations* in the $\mathtt{AT}_1$ and $\mathtt{AT}_2$ models and compare with the experiments gathered in Gómez et al. (2006). The core of their analysis consist in defining a generalized stress intensity factor

$$K_U = K_t \sigma_c^\infty \sqrt{\frac{\pi \rho}{4}}, \tag{13}$$

where K_t, the *notch stress concentration factor*, is a parameter depending on the local (a and ρ), as well as global sample geometry and loading. Through a dimensional analysis, they studied the dependence of the critical generalized stress intensity factor at the onset of fracture and the notch radius. We performed series of numerical simulations of double edge tension (DENT) experiments on a sample of length $h = 40$ for multiple values of the notch depth $a = 10$, spacing $b = 20$, radius $\rho = 2.5, 1.25,$ and 0.5 for which the value K_t, computed in Lazzarin and Filippi (2006) is respectively 5.33, 7.26, and 11.12. In each case, we leveraged the symmetries of the problem by performing computations with the $\mathtt{AT}_1$ and $\mathtt{AT}_2$ models on a quarter of the domain for a number of values of the internal length ℓ corresponding to ρ/ℓ_{ch} between 0.05 and 20. In all cases, undamaged notch boundary conditions were used.

In Fig. 13, we overlay the outcome of our simulations over the experimental results gathered in Gómez et al. (2006). As for the V-notch, we observe that the $\mathtt{AT}_2$ model performs poorly for weak stress concentrations (large values of ρ/ℓ_{ch}), as the lack of an elastic phase leads to the creation of large partially damaged areas. For sharp notches ($\rho \simeq 0$), our simulations concur with the experiments in predicting crack nucleation when $K_U = K_{Ic}$. As seen earlier, the $\mathtt{AT}_1$ slightly overestimates the critical load in this regime when undamaged notch boundary conditions are used. In light of Fig. 13, we claim that numerical simulations based on the variational phase-field model $\mathtt{AT}_1$ provides a simple way to predict crack nucleation that does not require the computation of a notch stress concentration factors K_t or the introduction of an ad-hoc criterion.

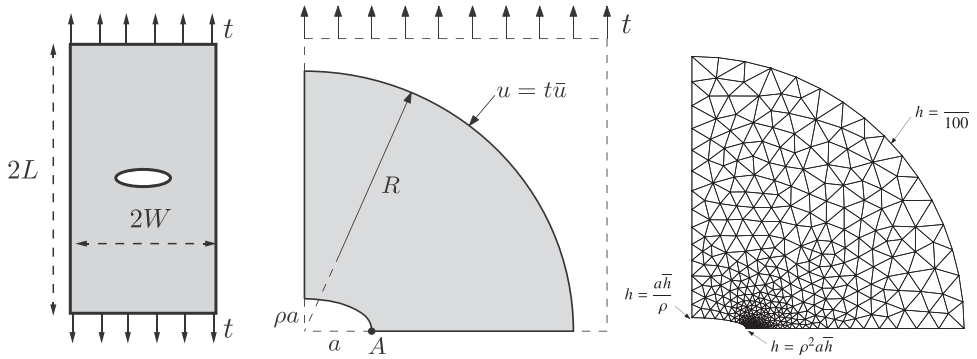

Fig. 14. Crack nucleation in an infinite domain containing an elliptical hole. (left) domain geometry (center) computational domain (right) typical mesh.

4. Size effects in variational phase-field models

Variational phase-field models are characterized by the intrinsic length ℓ, or ℓ_{ch}. In this section, we show that this length-scale introduces physically pertinent scale effects, corroborating its interpretation as a material length. To this end, we study the nucleation of a crack in the uniaxial traction of a plate $(-W, W) \times (-L, L)$ with a centered elliptical hole with semi-axes a and ρa $(0 \le \rho \le 1)$ along the x- and y-axes respectively, see Fig. 14. In Section 4.1, we study the effect of the size and shape of the cavity, assumed to be small with respect to the dimension of the plate ($a \ll W, L$). In Section 4.2, we investigate material and structural size effects for a plate of finite width in the limit case of a perfect crack ($\rho = 0$).

4.1. Effect of an elliptical cavity: size and shape effects

For a small hole ($a \ll W, L$), up to a change of scale, the problem can be fully characterized by two dimensionless parameters: a/ℓ, and ρ. For a linear elastic and isotropic material occupying an infinite domain, a close form expression of the stress field as a function of the hole size and aspect ratio is given in Inglis (1913). The stress is maximum at the points $A = (a, 0)$ and $A' = (-a, 0)$, where the radial stress is zero and the hoop stress is given by:

$$\sigma_{\max} = t\left(1 + \frac{2}{\rho}\right), \tag{14}$$

t denoting the applied tensile stress along the upper and lower edges of the domain, i.e. the applied macroscopic stress at infinity. We denote by $\bar{u}$ the corresponding displacement field for $t = 1$, which is given in Gao (1996).

As for the case of a perfect bar, (14) exposes a fundamental issue: if $\rho > 0$, the stress remains finite, so that Griffith–based theories will only predict crack nucleation if $\rho = 0$. In that case the limit load given by the Griffith's criterion for crack nucleation is

$$t = \sigma_G := \sqrt{\frac{G_c E'}{a\pi}}. \tag{15}$$

However, as $\rho \to 0$, the stress becomes singular so that the critical tensile stress σ_c is exceeded for an infinitesimally small macroscopic stress t.

Following the findings of the previous sections, we focus our attention on the $\mathtt{AT}_1$ model only, and present numerical simulations assuming a Poisson ratio $\nu = 0.3$ and plane-stress conditions. We perform our simulations in domain of finite size, here a disk of radius R centered around the defect. Along the outer perimeter of the domain, we apply a boundary displacement $u = t\bar{u}$, where $\bar{u}$ is as in Inglis (1913), and we use the macroscopic stress t a loading parameter. Assuming a symmetric solution, we perform our computations on a quarter of the domain. For the circular case $\rho = 1$, we use a reference mesh size $\bar{h} = \ell_{\min}/10$, where $\ell_{\min}$ is the smallest value of the internal length of the set of simulations. For $\rho < 1$, we selectively refine the element size near the expected nucleation site (see Fig. 14, right). In order to minimize the effect of the finite size of the domain, we set $R = 100a$.

We performed numerical simulations varying the aspect ratio a/ℓ from 0.1 to 50 and the ellipticity ρ from 0.1 to 1.0. In each case, we started from an undamaged state an monotonically increased the loading. In all numerical simulations, we observe two critical loading t_e and t_c, the *elastic limit* and *structural strength*, respectively. For $0 \le t < t_e$ the solution is purely elastic, *i.e.* the damage field α remains identically 0 (see Fig. 15, left). For $t_e \le t < t_c$, partial distributed damage is observed. The damage field takes its maximum value $\alpha_{\max} < 1$ near point A (see Fig. 15, center). At $t = t_c$, a fully developed crack nucleates, then propagates for $t > t_c$ (see Fig. 15, right). As for the Pac-Man problem, we identify the crack nucleation with a jump in surface energy, and focus on loading at the onset of damage.

From the one-dimensional problem of Section 2.2 and Pham et al. (2011a); 2011b), we expect damage nucleation to take place when the maximum stress $\sigma_{\max}$ reaches the nominal material strength $\sigma_c = \sqrt{3G_c E'/8\ell}$ (see Table 1), i.e. for a critical

Fig. 15. Damage field at the boundary of the hole in the elastic phase $0 < t < t_e$ (left), the phase with partial damage $t_e < t < t_c$ (center), and after the nucleation of a crack $t > t_c$ (right). Blue: $\alpha = 0$, red: $\alpha = 1$. The simulation is for $\rho = 1.0$ and $a/\ell = 5$. (For interpretation of the references to colour in this figure legend, the reader is referred to the web version of this article.)

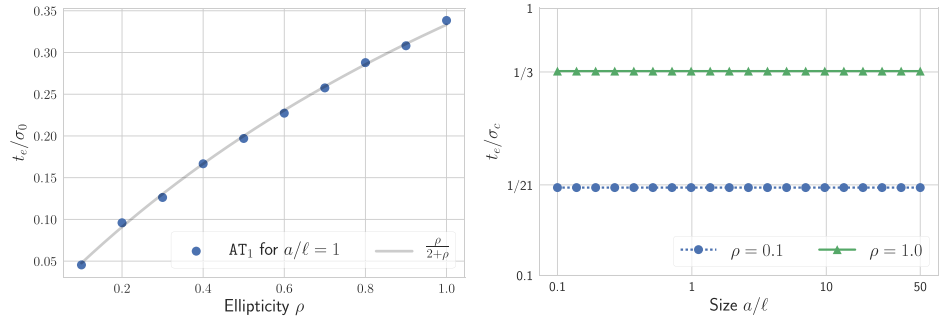

Fig. 16. Normalized applied macroscopic stress t_e/σ_c at damage initiation as a function of the aspect ratio ρ for $a/\ell = 1$ (left) and of the relative defect sizes a/ℓ for $\rho = 1$ and $\rho = 0.1$ (right).

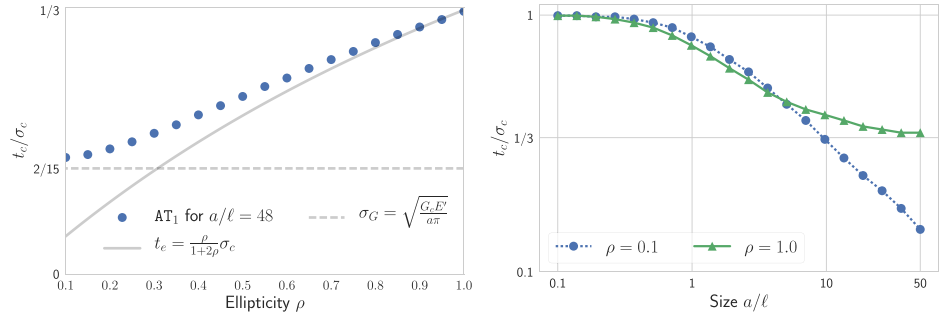

Fig. 17. Normalized applied macroscopic stress t_c/σ_e at crack nucleation for an elliptic cavity in an infinite plate. Left: shape effect for cavities of size much larger than the internal length ($a/\ell = 48$); the solid line is the macroscopic stress at the damage initiation t_e (see also Fig. 16) and dots are the numerical results for the AT$_1$ model. Right: size effect for circular ($\rho = 1.0$) and highly elongated ($\rho = 0.1$) cavities.

load

$$t_e = \frac{\rho}{2+\rho}\sigma_c = \frac{\rho}{2+\rho}\sqrt{\frac{3G_cE'}{8\ell}}. \tag{16}$$

Fig. 16 (left) confirms this expectation by comparing the ratio t_e/σ_c to its expected value $\rho/(2+\rho)$ for ρ ranging from 0.1 to 1. Fig. 16(right) highlights the absence of size effect on the damage nucleation load, by comparing t_e/σ_c for multiple values of a/ℓ while keeping ρ fixed at 0.1 and 1.

Fig. 17 focuses on the crack nucleation load t_c, showing its dependence on the defect shape (left) and size (right). Fig. 17(right) shows the case of circular hole ($\rho = 1$) and an elongated ellipse, which can be identified to a crack ($\rho = 0.1$). It clearly highlights a scale effect including three regimes:

i. For "small" holes ($a \ll \ell$), crack nucleation takes place when $t = \sigma_c$, as in the uniaxial traction of a perfect bar without the hole: the hole has virtually no effect on crack nucleation. In this regime the strength of a structure is completely determined by that of the constitutive material. Defects of this size do not reduce the structural strength and can be ignored at the macroscopic level.

ii. Holes with length of the order of the internal length ($a = \mathcal{O}(\ell)$), have a strong impact on the structural strength. In this regime the structural strength can be approximated by

$$\log(t_c/\sigma_c) = D\log(a/\ell) + c, \tag{17}$$

where D is an dimensionless coefficient depending on the defect shape. For a circular hole $\rho = 1$, we have $D \approx -1/3$.

iii. When $a \gg \ell$, the structural failure is completely determined by the stress distribution surrounding the defect. We observe that for weak stress singularities ($\rho \equiv 1$), nucleation takes place when the maximum stress reaches the elastic limit σ_e, whereas the behavior as $\rho \equiv 0$ is consistent with Griffith criterion, *i.e.* the nucleation load scales as $1/\sqrt{a}$.

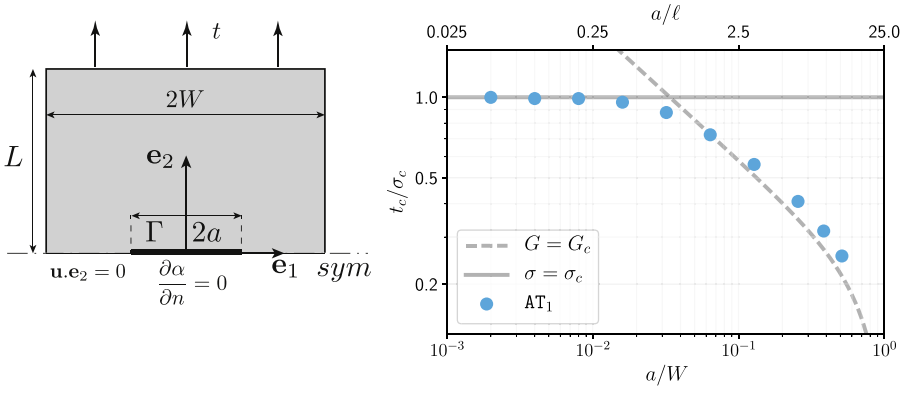

Fig. 18. Initiation of a crack of length $2a$ in a plate of finite width $2W$. The numerical results (dots) are obtained with the $\mathtt{AT}_1$ model for $\ell = W/25$. The strength criterion and the Griffith's criterion (18).

Fig. 17 (right) shows that the shape of the cavity has a significant influence on the critical load only in the latter regime, $a \gg \ell$. Indeed, for a/ℓ of the order of the unity or smaller, the critical loads t_c for circular and highly elongated cavities are almost indistinguishable. This small sensitivity of the critical load on the shape is the result of the stress-smoothing effect of the damage field, which is characterized by a cut-off length of the order of ℓ. Fig. 17 (left) shows the critical stress t_c at nucleation when varying the aspect ratio ρ for $a/\ell = 48$, for which $\sigma_G/\sigma_c = 2/15$. As expected, the critical stress varies smoothly from the value σ_G (15) predicted by the Griffith theory for a highly elongated cavity identified to a perfect crack, to t_e (16) for circular cracks, where the crack nucleates as soon as the maximum stress $\sigma_{\max}$ attains the elastic limit.

This series of experiments is consistent with the results of Section 3.2 showing that variational phase-field models are capable of simultaneously accounting for critical elastic energy release rate and critical stress. Furthermore, they illustrate how the internal length ℓ can be linked to critical defect size as the nucleation load for a vanishing defect of size less than ℓ approaches that of a flawless structure.

4.2. Competition between material and structural size effects

We can finally conclude the study of size effects in variational phase-field models by focusing on the competition between material and structural size effects. For that matter, we study the limit case $\rho = 0$ of a perfect crack of finite length $2a$ in a plate of finite width $2W$ (see Fig. 18-left). Under the hypotheses of LEFM, the critical load upon which the crack propagates is

$$\sigma_G(a/\ell_{ch}, a/W) = \sqrt{\frac{G_c E' \cos(\frac{a\pi}{2W})}{a\pi}} = \sigma_c \sqrt{\frac{1}{\pi}\frac{\ell_{ch}}{a}\cos\left(\frac{a\pi}{2W}\right)}, \tag{18}$$

which reduces to (15) for large plate ($W/a \to \infty$). As before, we note that $\sigma_G/\sigma_c \to \infty$ as $a/\ell_{ch} \to 0$, so that for any given load, the material's tensile strength is exceeded for short enough initial crack.

We performed series of numerical simulations using the $\mathtt{AT}_1$ model on a quarter of the domain with $W = 1$, $L = 4$, $\nu = 0.3$, $\ell = W/25$, $h = \ell/20$, and the initial crack's half-length a ranging from 0.025ℓ to 12.5ℓ (i.e. $0.001W$ to $0.5W$). The pre-existing crack was modeled as a geometric feature and undamaged crack lip boundary conditions were prescribed. The loading was applied by imposing a uniform normal stress of amplitude t to its upper and lower edge.

Fig. 18, displays the normalized macroscopic structural strength of the sample, t_c/σ_c, where σ_c is given by (6), and t_c is the applied load upon which the crack grows, identified as before. The results are in good agreement with classical theories linking size-effect on the strength of the material (Bažant, 2005). When $a \gg \ell$, *i.e.* when the defect is large compared to the material's length, crack initiation is governed by Griffith's criterion (18). As noted earlier, the choice of undamaged notch boundary conditions on the damage fields leads to slightly overestimating the nucleation load. Our numerical simulations reproduce the structural size effect predicted by LEFM when the crack length is comparable to the plate width W.

When $a \ll \ell$, we observe that the macroscopic structural strength is very close to the material's tensile strength. Again, below the material's internal length, defects have virtually no impact on the structural response. LEFM and Griffith-based models cannot account for this material size-effect. These effects are introduced in variational phase-field model by the additional material parameter ℓ.

In the intermediate regime $a = \mathcal{O}(\ell)$, we observe a smooth transition between strength and toughness criteria, where the tensile strength is never exceeded.

When $a \gg \ell$, our numerical simulations are consistent with predictions from LEFM shown as a dashed line in Fig. 18, whereas when $a \ll \ell$, the structural effect of the small crack disappear, and nucleation takes place at or near the material's tensile strength, *i.e.* $t_c/\sigma_c \simeq 1$.

5. Conclusion

In contrast with most of the literature on phase-field models of fracture focusing validation and verification in the context of propagation "macroscopic" cracks (Mesgarnejad et al., 2015; Pham et al., 2017), we have studied crack nucleation and initiation in multiple geometries. We confirmed observations reported elsewhere in the literature that although they are mathematically equivalent in the limit of $\ell \to 0$, damaged notch boundary conditions lead to a more accurate computation near strong stress singularities whereas away from singularities, undamaged notch boundary conditions are to be used. Our numerical simulations also highlight the superiority of phase-field models such as $\mathtt{AT}_1$ which exhibit an elastic phase in the one-dimensional tension problem over those who don't (such as $\mathtt{AT}_2$), when nucleation away from strong singularity is involved. Our numerical simulations suggest that it is not possible to accurately account for crack nucleation near "weak" singularities using the $\mathtt{AT}_2$ model. We infer that a strictly positive elastic limit σ_e is a required feature of a phase-field model that properly account for crack nucleation.

We have shown that as suggested by the one-dimensional tension problem, the regularization parameter ℓ must be understood (up to a model-dependent multiplicative constant) as the material's characteristic or internal length $\ell_{ch} = G_c E/\sigma_c^2$, and linked to the material strength σ_c. With this adjustment, we show that variational phase-field models are capable of quantitative prediction of crack nucleation in a wide range of geometries including three- and four-point bending with various type of notches, single and double edge notch tests, and a range of brittle materials, including steel and Duraluminium at low temperatures, PVC foams, PMMA, and several ceramics.

We recognize that measuring a material's tensile strength is difficult and sensitive to the presence of defect, so that formulas (6) may not be a practical way of computing a material's internal length. Instead, we propose to perform series of experiments such as three point bending with varying notch depth, radius or angle, as we have demonstrated in Fig. 11 that with a properly adjusted internal length, variational phase-field models are capable of predicting the nucleation load for any notch depth or aperture. Furthermore, since variational phase-field models do not rely on any crack-tip asymptotic, this identification can be made even in situation where generalized stress or notch intensity factors are not known, or are affected by the sample's structural geometry.

We have also shown that variational phase-field models properly account for size effects that cannot be recovered from Griffith-based theories. By introducing the material's internal length, they can account for the vanishing effect of small defects on the structural response of a material, or reconcile the existence of a critical material strength with the existence of stress singularity. Most importantly, they do not require introducing ad-hoc criteria based on local geometry and loading. On the contrary, we see that in most situation, criteria derived from the asymptotic analysis of a micro-geometry can be recovered *a posteriori*. Furthermore, variational phase-field models are capable of quantitative prediction of crack path after nucleation. Again, they do so without resolving to introducing additional ad-hoc criteria, but only relying on a general energy minimization principle.

In short, we have demonstrated that variational phase-field models address some of the most vexing issues associated with brittle fracture: scale effects, nucleation, existence of a critical stress, and path prediction.

Of course, there are still remaining issues that need to be addressed. Whereas the models are derived from irreversibility, stability and energy balance, our numerical simulations do not enforce energy balance as indicated by a drop of the total energy upon crack nucleation without string singularities. Note that to this day, devising an evolution principle combining the strength of (3) while ensuring energy balance is still an open problem. Perhaps extensions into phase field models dynamic fracture will address this issue.

Fracture in compression remains an issue in variational phase-field models. Although several approaches have been proposed that typically consist in splitting the strain energy into a damage inducing and non damage inducing terms, neither of the proposed splits are fully satisfying (see Amor et al., 2009; Lancioni and Royer-Carfagni, 2009; Li, 2016 for instance). In particular, it is not clear of either of this models is capable of simultaneously accounting for nucleation under compression and self-contact.

Finally, even though a significant amount of work has already been invested in extending the scope of phase-field models of fracture beyond perfectly brittle materials, to our knowledge, none of the proposed extensions has demonstrated its predictive power yet.

Acknowledgments

This material is based upon work supported by the National Science Foundation under Grant Nos. DMS-1312739 and DMS-1535076. This work used the Extreme Science and Engineering Discovery Environment (XSEDE), which is supported by National Science Foundation grant number ACI-1548562. Portions of this research were conducted with high performance computing resources provided by Louisiana State University (http://www.hpc.lsu.edu) and by the Institute for Computing and Data Sciences (ISCD) of University Pierre et Marie Curie (http://www.iscd.upmc.fr). C.M. acknowledges the support of the project ANR-11-LABX-0037 (Agence Nationale de la Recherche) and of Sorbonnes Universités project FRZX026-SU-16-R-EMR-02-ANIS.

Appendix A. Tables of experimental an numerical data for V-notch experiments

Table A.3
Critical generalized stress intensity factor k for crack nucleation at a notch as a function of the notch opening angle $\tilde{\omega}$ from Fig. 5. Results for the $\mathtt{AT}_1$ and $\mathtt{AT}_2$ models with damaged -D and undamaged -U notch lips conditions. The results are obtained with numerical simulations on the Pac-Man geometry with $(K_{Ic})_{\text{eff}} = 1$ and $\ell = 0.01$ so that $\sigma_c = 10$ under plane-strain conditions with a unit Young's modulus and a Poisson ratio $\nu = 0.3$.

ω	λ	k_c ($\mathtt{AT}_1$-U)	k_c ($\mathtt{AT}_1$-D)	k_c ($\mathtt{AT}_2$-U)	k_c ($\mathtt{AT}_2$-D)
0.01°	0.500	1.292	1.084	1.349	1.284
10.0°	0.500	1.308	1.091	1.328	1.273
20.0°	0.503	1.281	1.121	1.376	1.275
30.0°	0.512	1.359	1.186	1.397	1.284
40.0°	0.530	1.432	1.306	1.506	1.402
50.0°	0.563	1.636	1.540	1.720	1.635
60.0°	0.616	2.088	1.956	2.177	2.123
70.0°	0.697	2.955	2.704	3.287	3.194
80.0°	0.819	4.878	4.391	5.629	5.531
85.0°	0.900	6.789	5.890	7.643	7.761
89.9°	0.998	9.853	8.501	9.936	9.934

Table A.4
Generalized critical stress intensity factors as a function of the notch aperture in soft annealed tool steel, (AISI O1 at -50°C). Experimental measurements from Strandberg (2002) using SENT and TPB compared with Pac-Man simulations with the $\mathtt{AT}_1$ model.

$2\tilde{\omega}$	Type	Experiments		Undamaged notch		Damaged notch	
		$k_c^{(exp)}$	stdev	$k_c^{(num)}$	Rel. error	$k_c^{(num)}$	Rel. error
0°	TPB	51.77	3.06	67.09	22.84%	54.69	5.35 %
30°	SENT	60.97	1.97	66.91	8.88 %	56.99	6.98 %
60°	SENT	65.81	1.52	69.55	5.39 %	62.95	4.53 %
90°	TPB	88.62	3.58	85.16	4.06 %	78.15	13.40%
120°	SENT	142.74	2.25	130.81	9.12 %	121.68	17.30%
140°	SENT	243.73	31.86	211.06	15.48%	191.91	27.00%

Table A.5
Generalized critical stress intensity factors as a function of the notch aperture in Divinycell® PVC foam. Experimental measurements from Grenestedt et al. (1996) using four point bending compared with Pac-Man simulations with the $\mathtt{AT}_1$ model.

$2\tilde{\omega}$	Mat	Experiments		Undamaged notch		Damaged notch	
		$k_c^{(exp)}$	stdev	$k_c^{(num)}$	Rel. error	$k_c^{(num)}$	Rel. error
0°	H80	0.14	0.01	0.18	22.91%	0.15	5.81%
	H100	0.26	0.02	0.34	24.62%	0.28	7.61%
	H130	0.34	0.01	0.44	29.34%	0.36	5.09%
	H200	0.57	0.02	0.74	47.60%	0.61	6.53%
90°	H80	0.20	0.02	0.22	12.65%	0.21	4.73%
	H100	0.36	0.02	0.41	12.29%	0.38	4.10%
	H130	0.49	0.05	0.54	11.33%	0.50	0.50%
	H200	0.81	0.08	0.91	20.54%	0.83	2.21%
140°	H80	0.53	0.06	0.53	0.37%	0.48	9.26%
	H100	0.89	0.04	0.92	3.43%	0.84	5.91%
	H130	1.22	0.10	1.25	2.95%	1.13	7.48%
	H200	2.02	0.14	2.07	4.92%	1.89	6.80%
155°	H80	0.86	0.07	0.83	3.63%	0.75	14.36%
	H100	1.42	0.08	1.42	0.14%	1.29	10.63%
	H130	1.90	0.10	1.95	2.82%	1.76	8.06%
	H200	3.24	0.15	3.23	0.89%	2.92	11.02%

Table A.6
Generalized critical stress intensity factors as a function of the notch aperture in Duraluminium. Experimental measurements from Seweryn (1994) using single edge notch tension compared with Pac-Man simulations with the AT_1 model.

$\bar{\omega}$	Type	Experiments		Undamaged notch		Damaged notch	
		$k_c^{(exp)}$	stdev	$k_c^{(num)}$	Rel. error	$k_c^{(num)}$	Rel. error
10°	DENT	53.55	0.94	64.80	17.36%	56.40	5.05%
20°	DENT	57.10	0.26	65.11	12.30%	58.52	2.43%
30°	DENT	60.50	0.60	67.17	9.94%	62.11	2.59%
40°	DENT	66.34	0.50	74.07	10.44%	69.24	4.18%
50°	DENT	80.15	0.46	86.61	7.46%	82.25	2.55%
60°	DENT	102.00	1.17	114.20	10.69%	107.43	5.05%
70°	DENT	150.44	1.17	170.19	11.61%	158.91	5.33%
80°	DENT	291.75	1.94	305.03	4.35%	274.74	6.19%
90°	DENT	705.27	8.53	661.19	6.67%	592.59	19.01%

Table A.7
Generalized critical stress intensity factors as a function of the notch aperture in PMMA. Experimental measurements from Seweryn (1994) using single edge notch tension compared with Pac-Man simulations with the AT_1 model.

$\bar{\omega}$	Type	Experiments		Undamaged notch		Damaged notch	
		$k_c^{(exp)}$	stdev	$k_c^{(num)}$	Rel. error	$k_c^{(num)}$	Rel. error
10°	DENT	1.87	0.03	2.50	25.29%	2.07	10.03%
20°	DENT	1.85	0.03	2.53	26.89%	2.13	12.97%
30°	DENT	2.17	0.03	2.65	18.17%	2.33	6.92%
40°	DENT	2.44	0.02	3.07	20.65%	2.73	10.70%
50°	DENT	3.06	0.05	3.94	22.31%	3.54	13.63%
60°	DENT	4.35	0.18	5.95	26.97%	5.41	19.69%
70°	DENT	8.86	0.18	11.18	20.74%	10.10	12.26%
80°	DENT	28.62	0.68	27.73	3.20%	24.55	16.56%
90°	DENT	104.85	10.82	96.99	8.11%	85.37	22.82%

Table A.8
Generalized critical stress intensity factors as a function of the notch aperture in Aluminium oxide ceramics. Experimental measurements from Yosibash et al. (2004) using three and four point bending compared with Pac-Man simulations.

$2\bar{\omega}$	type	Experiments		Undamaged notch		Damaged notch	
		$k_c^{(exp)}$	stdev	$k_c^{(num)}$	Rel. error	$k_c^{(num)}$	Rel. error
30°	TPB	4.49	0.57	4.97	9.6%	4.53	0.9%
	FPB	4.24	0.30	4.97	14.6%	4.53	6.4%
60°	TPB	6.02	n/a	5.35	12.6%	5.00	20.3%
	FPB	5.14	0.09	5.35	3.8%	5.00	2.8%
90°	TPB	6.66	0.50	6.99	4.8%	6.72	1.0%
	FPB	6.81	0.54	6.99	2.6%	6.72	1.3%
120°	TPB	13.21	0.87	13.12	0.7%	12.38	6.8%
	FPB	14.66	1.23	13.12	11.7%	12.38	18.4%

Table A.9
Generalized critical stress intensity factors as a function of the notch aperture in PMMA. Experimental measurements from Dunn et al. (1997) using three and four point bending compared with Pac-Man simulations. The value a/h refers to the ratio depth of the notch over sample thickness. See Fig. 9 for geometry and loading.

$2\bar{\omega}$	a/h	Experiments		Undamaged notch		Damaged notch	
		$k_c^{(exp)}$	stdev	$k_c^{(num)}$	Rel. error	$k_c^{(num)}$	Rel. error
60°	0.1	1.41	0.02	1.47	4.5%	1.29	9.3%
	0.2	1.47	0.04	1.47	0.4%	1.29	14.0%
	0.3	1.28	0.03	1.47	13.0%	1.29	0.4%
	0.4	1.39	0.04	1.47	5.8%	1.29	7.8%
90°	0.1	2.04	0.02	1.98	3.0%	1.81	12.9%
	0.2	1.98	0.01	1.98	0.0%	1.81	9.6%
	0.3	2.08	0.03	1.98	5.1%	1.81	15.2%
	0.4	2.10	0.03	1.98	5.9%	1.81	16.1%
120°	0.1	4.15	0.02	3.87	7.3%	3.63	14.3%
	0.2	4.03	0.06	3.87	4.2%	3.63	11.0%
	0.3	3.92	0.18	3.87	1.4%	3.63	8.0%
	0.4	3.36	0.09	3.87	13.0%	3.63	7.4%

Table A.10
Critical load reported in Yosibash et al. (2004) using three- and four-point bending experiments of an Al_2O_3–7%ZrO_2 sample compared with numerical simulations using the AT_1 model and undamaged notch boundary conditions. TPB and FPB refer respectively to three point bending and four point bending. See Fig. 9 for geometry and loading.

$2\tilde{\omega}$	Type	$P_c^{(exp)}$[N]	stdev	$P_c^{(num)}$[N]	Rel. error
30°	TPB	1470.50	72.01	1517.59	3.1%
	FPB	1726.00	56.29	1976.59	12.7%
60°	TPB	1736.00	0.00	1517.59	14.4%
	FPB	1909.17	60.88	1986.62	3.9%
90°	TPB	1528.40	149.41	1608.04	5.0%
	FPB	2024.40	212.03	2127.09	4.8%
120°	TPB	1933.00	75.15	1949.75	0.9%
	FPB	2711.29	187.66	2618.73	3.5%

Table A.11
Load at failure reported in Yosibash et al. (2004) using three point bending experiments of a PMMA sample compared to full domain numerical simulations using the AT_1 model with undamaged notch boundary conditions. The value a/h refers to the ratio depth of the notch over sample thickness. See Fig. 9 for geometry and loading.

$2\tilde{\omega}$	a/h	$P_c^{(exp)}$ [N]	stdev	$P_c^{(num)}$ [N]	Rel. error
60°	0.1	608.50	6.69	630.81	3.5%
	0.2	455.75	12.48	451.51	0.9%
	0.3	309.00	8.19	347.98	11.2%
	0.4	258.75	6.61	268.69	3.7%
90°	0.1	687.33	5.19	668.69	2.8%
	0.2	491.00	2.94	491.41	0.1%
	0.3	404.33	5.44	383.33	5.5%
	0.4	316.00	4.24	297.48	6.2%
120°	0.1	881.75	4.60	822.22	7.2%
	0.2	657.25	9.36	632.32	3.9%
	0.3	499.60	25.41	499.50	0.0%
	0.4	336.25	9.09	386.87	13.1%

References

Abdollahi, A., Arias, I., 2012. Phase-field modeling of crack propagation in piezoelectric and ferroelectric materials with different electromechanical crack conditions. J. Mech. Phys. Solids 60 (12), 2100–2126. doi:10.1016/j.jmps.2012.06.014.

Alessi, R., Marigo, J.-J., Vidoli, S., 2014. Gradient damage models coupled with plasticity and nucleation of cohesive cracks. Arch. Rat. Mech. Anal. 214 (2), 575–615. doi:10.1007/s00205-014-0763-8.

Ambati, M., Gerasimov, T., De Lorenzis, L., 2015a. Phase-field modeling of ductile fracture. Comput. Mech. 55 (5), 1017–1040. doi:10.1007/s00466-015-1151-4.

Ambati, M., Kruse, R., De Lorenzis, L., 2015b. A phase-field model for ductile fracture at finite strains and its experimental verification. Comput. Mech. 57 (1), 149–167. doi:10.1007/s00466-015-1225-3.

Ambrosio, L., Tortorelli, V.M., 1990. Approximation of functionals depending on jumps by elliptic functionals via Γ-convergence. Commun. Pure Appl. Math. 43 (8), 999–1036.

Ambrosio, L., Tortorelli, V.M., 1992. On the approximation of free discontinuity problems. Boll. Un. Mater. Ital. B (7) 6 (1), 105–123.

Amor, H., Marigo, J.-J., Maurini, C., 2009. Regularized formulation of the variational brittle fracture with unilateral contact: numerical experiments. J. Mech. Phys. Solids 57 (8), 1209–1229. doi:10.1016/j.jmps.2009.04.011.

Balay, S., Abhyankar, S., Adams, M.F., Brown, J., Brune, P., Buschelman, K., Dalcin, L., Eijkhout, V., Gropp, W.D., Kaushik, D., Knepley, M.G., McInnes, L.C., Rupp, K., Smith, B.F., Zampini, S., Zhang, H., Zhang, H., 2016. PETSc Users Manual. Technical Report, ANL-95/11 – Revision 3.7. Argonne National Laboratory.

Balay, S., Abhyankar, S., Adams, M. F., Brown, J., Brune, P., Buschelman, K., Dalcin, L., Eijkhout, V., Gropp, W. D., Kaushik, D., Knepley, M. G., McInnes, L. C., Rupp, K., Smith, B. F., Zampini, S., Zhang, H., Zhang, H., 2017. PETSc Web page.

Balay, S., Gropp, W., Curfman McInnes, L., Smith, B., 1997. Efficient management of parallelism in object oriented numerical software libraries. In: Arge, E., Bruaset, A.M., Langtangen, H.P. (Eds.), Modern Software Tools in Scientific Computing. Birkhäuser Press, pp. 163–202.

Bažant, Z.P., 1997. Scaling of quasibrittle fracture: asymptotic analysis. Int. J. Fract. 83 (1), 19–40.

Bažant, Z.P., 2005. Scaling of Structural Strength, 2nd edition Elsevier.

Bellettini, G., Coscia, A., 1994. Discrete approximation of a free discontinuity problem. Numer. Funct. Anal. Optim. 15 (3–4), 201–224.

Benallal, A., Marigo, J.-J., 2007. Bifurcation and stability issues in gradient theories with softening. Model. Simul. Mater. Sc. 15 (1), S283.

Borden, M.J., Hughes, T.J.R., Landis, C.M., Anvari, A., Lee, I.J., 2016. A phase-field formulation for fracture in ductile materials: finite deformation balance law derivation, plastic degradation, and stress triaxiality effects. Comp. Meth. Appl. Mech. Eng. 312, 130–166. doi:10.1016/j.cma.2016.09.005.

Borden, M.J., Verhoosel, C.V., Scott, M.A., Hughes, T.J., Landis, C.M., 2012. A phase-field description of dynamic brittle fracture. Comput. Methods Appl. Mech. Eng. 217–220 (0), 77–95. doi:10.1016/j.cma.2012.01.008.

de Borst, R., Gutiérrez, M., Wells, G., Remmers, J., Askes, H., 2004. Cohesive-zone models, higher-order continuum theories and reliability methods for computational failure analysis. Int. J. Numer. Meth. Eng. 60, 289–315.

Bourdin, B., 1999. Image segmentation with a finite element method. M2AN Math. Model. Numer. Anal. 33 (2), 229–244.

Bourdin, B., 2007. Numerical implementation of a variational formulation of quasi-static brittle fracture. Interfaces Free Bound. 9, 411–430.

Bourdin, B., Chambolle, A., 2000. Implementation of an adaptive finite-element approximation of the Mumford-Shah functional. Numer. Math. 85 (4), 609–646.

Bourdin, B., Chukwudozie, C., Yoshioka, K., 2012. A variational approach to the numerical simulation of hydraulic fracturing. In: Proceedings of the 2012 SPE Annual Technical Conference and Exhibition, SPE 159154.

Bourdin, B., Francfort, G.A., Marigo, J.-J., 2000. Numerical experiments in revisited brittle fracture. J. Mech. Phys. Solids 48 (4), 797–826.
Bourdin, B., Francfort, G.A., Marigo, J.-J., 2008. The variational approach to fracture. J. Elasticity 91 (1–3), 5–148.
Bourdin, B., Larsen, C.J., Richardson, C., 2011. A time-discrete model for dynamic fracture based on crack regularization. Int. J. Fracture 168, 133–143. doi:10.1007/s10704-010-9562-x.
Bourdin, B., Marigo, J.-J., Maurini, C., Sicsic, P., 2014. Morphogenesis and propagation of complex cracks induced by thermal shocks. Phys. Rev. Lett. 112 (1), 014301. doi:10.1103/PhysRevLett.112.014301.
Braides, A., 1998. Approximation of Free-Discontinuity Problems. Lecture Notes in Mathematics, 1694. Springer.
Braides, A., 2002. Γ-convergence for beginners. Oxford Lecture Series in Mathematics and its Applications, 22. Oxford University Press, Oxford.
Burke, S., Ortner, C., Süli, E., 2010. An adaptive finite element approximation of a variational model of brittle fracture. SIAM J. Numer. Anal. 48 (3), 980–1012. doi:10.1137/080741033.
Burke, S., Ortner, C., Süli, E., 2013. An adaptive finite element approximation of a generalized Ambrosio-Tortorelli functional. Math. Mod. Meth. Appl. S. 23 (9), 1663–1697.
Chambolle, A., 2004. An approximation result for special functions with bounded variations. J. Math Pures Appl. 83, 929–954.
Chambolle, A., 2005. Addendum to “an approximation result for special functions with bounded deformation” [j. math. pures appl. (9) 83 (7) (2004) 929–954]: the n-dimensional case. J. Math Pures Appl. 84, 137–145.
Charlotte, M., Laverne, J., Marigo, J.-J., 2006. Initiation of cracks with cohesive force models: a variational approach. Eur. J. Mech. A/Solids 25 (4), 649–669. doi:10.1016/j.euromechsol.2006.05.002.
Chudnovsky, A., 2014. Slow crack growth, its modeling and crack-layer approach: a review. Int. J. Eng. Sci. 83, 6–41. doi:10.1016/j.ijengsci.2014.05.015.
Chukwudozie, C., 2016. Application of the Variational Fracture Model to Hydraulic Fracturing in Poroelastic Media. Louisiana State University Ph.D. thesis. Craft & Hawkins Department of Petroleum Engineering
Conti, S., Focardi, M., Iurlano, F., 2016. Phase field approximation of cohesive fracture models. Ann. I. H. Poincaré - AN 33 (4), 1033–1067. doi:10.1016/j.anihpc.2015.02.001. Preprint.
Crismale, V., Lazzaroni, G., 2016. Viscous approximation of quasistatic evolutions for a coupled elastoplastic-damage model. Calc. Var. Partial Dif. 55 (17), 1–54. doi:10.1007/s00526-015-0947-6.
Dal Maso, G., 1993. An Introduction to Γ-convergence. Birkhäuser, Boston.
Del Piero, G., 2013. A variational approach to fracture and other inelastic phenomena. J. Elasticity 112 (1), 3–77. doi:10.1007/s10659-013-9444-3.
Del Piero, G., Lancioni, G., March, R., 2013. A diffuse cohesive energy approach to fracture and plasticity: the one-dimensional case. J. Mech. Phys. Solids 8 (2–4), 109–151.
Destuynder, P., Djaoua, M., 1981. Sur une interprétation mathématique de l’intégrale de Rice en théorie de la rupture fragile. Math. Methods Appl. Sci. 3 (1), 70–87.
Dunn, M.L., Suwito, W., Cunningham, S., 1997. Fracture initiation at sharp notches: correlation using critical stress intensities. Int. J. Solids Struct. 34 (29), 3873–3883.
Falk, M.L., Needleman, A., Rice, J.R., 2001. A critical evaluation of cohesive zone models of dynamic fracture. J. Phys IV 11 (PR5), 43–50.
Francfort, G.A., Marigo, J.-J., 1998. Revisiting brittle fracture as an energy minimization problem. J. Mech. Phys. Solids. 46 (8), 1319–1342.
Fraternali, F., 2007. Free discontinuity finite element models in two-dimensions for in-plane crack problems. Theor. Appl. Fract. Mech. 47 (3), 274–282. doi:10.1016/j.tafmec.2007.01.006.
Freddi, F., Royer Carfagni, G., 2010. Regularized variational theories of fracture: a unified approach. J. Mech. Phys. Solids 58 (8), 1154–1174. doi:10.1016/j.jmps.2010.02.010.
Freddi, F., Iurlano, F., 2017. Numerical insight of a variational smeared approach to cohesive fracture. J. Mech. Phys. Solids 98, 156–171. doi:10.1016/j.jmps.2016.09.003.
Frémond, M., Nedjar, B., 1996. Damage, gradient of damage and principle of virtual power. Int. J. Solids Struct. 33 (8), 1083–1103.
Gao, X.-L., 1996. A general solution of an infinite elastic plate with an elliptic hole under biaxial loading. Int. J. Pres. Ves. Pip. 67 (1), 95–104.
Giacomini, A., 2005. Ambrosio-Tortorelli approximation of quasi-static evolution of brittle fractures. Calc. Var. Partial Diff. 22 (2), 129–172.
Giacomini, A., Ponsiglione, M., 2003. A discontinuous finite element approximation of quasi-static growth of brittle fractures. Numer. Funct. Anal. Optim. 24 (7–8), 813–850.
Gómez, F.J., Elices, M., 2003. A fracture criterion for sharp V-notched samples. Int J. Fracture 123, 163–175.
Gómez, F.J., Guinea, G.V., Elices, M., 2006. Failure criteria for linear elastic materials with U-notches. Int. J. Fracture 141 (1), 99–113. doi:10.1007/s10704-006-0066-7.
Gou, K., Mallikarjuna, M., Rajagopal, K.R., Walton, J.R., 2015. Modeling fracture in the context of a strain-limiting theory of elasticity: a single plane-strain crack. Int. J. Eng. Sci. 88, 73–82. doi:10.1016/j.ijengsci.2014.04.018.
Grenestedt, J.L., Hallström, S., Kuttenkeuler, J., 1996. On cracks emanating from wedges in expanded PVC foam. Eng. Fract. Mech. 54 (4), 445–456.
Griffith, A.A., 1921. The phenomena of rupture and flow in solids. Philos. Trans. R. Soc. S-A 221, 163–198.
Halphen, B., Nguyen, Q.S., 1975. Sur les matériaux standards généralisés. J. Mécanique 14 (1), 39–63.
Hofacker, M., Miehe, C., 2013. A phase field model of dynamic fracture: robust field updates for the analysis of complex crack patterns. Int. J. Num. Meth. Engng. 93 (3), 276–301. doi:10.1002/nme.4387.
Hossain, M.Z., Hsueh, C.-J., Bourdin, B., Bhattacharya, K., 2014. Effective toughness of heterogeneous media. J. Mech. Phys. Solids 71, 320–348.
Inglis, C.E., 1913. Stresses in plates due to the presence of cracks and sharp corners. Transactions of the Institute of Naval Architects 55, 219–241.
Issa, M.A., Issa, M.A., Islam, M.S., Chudnovsky, A., 2000. Size effects in concrete fracture: part i, experimental setup and observations. Int J. Fract. 102 (1), 1–24.
Iurlano, F., 2014. A density result for GSBD and its application to the approximation of brittle fracture energies. Calc. Var. Partial Diff. 51 (1/2), 315–342.
Karma, A., Kessler, D.A., Levine, H., 2001. Phase-field model of mode III dynamic fracture. Phys. Rev. Lett. 87 (4). doi:10.1103/PhysRevLett.87.045501.
Klinsmann, M., Rosato, D., Kamlah, M., McMeeking, R.M., 2015. An assessment of the phase field formulation for crack growth. Comp. Meth. Appl. Mech. Engng. 294, 313–330. doi:10.1016/j.cma.2015.06.009.
Lancioni, G., Royer-Carfagni, G., 2009. The variational approach to fracture: a practical application to the french *panthéon*. J. Elasticity 95 (1–2), 1–30.
Larsen, C.J., Ortner, C., Süli, E., 2010. Existence of solutions to a regularized model of dynamic fracture. Math. Models Methods Appl. Sci. 20 (7), 1021–1048. doi:10.1142/S0218202510004520.
Lazzarin, P., Filippi, S., 2006. A generalized stress intensity factor to be applied to rounded v-shaped notches. Int. J. Solids Struct. 43 (9), 2461–2478. doi:10.1016/j.ijsolstr.2005.03.007.
Leguillon, D., 2002. Strength or toughness? a criterion for crack onset at a notch. Euro. J. Mech. A/Solids 21 (1), 61–72.
Leguillon, D., Sanchez-Palencia, E., 1987. Computation of Singular Solutions in Elliptic Problems and Elasticity. John Wiley & Sons, Inc.
Li, B., Peco, C., Millán, D., Arias, I., Arroyo, M., 2014. Phase-field modeling and simulation of fracture in brittle materials with strongly anisotropic surface energy. Int. J. Numer. Meth. Eng. 102 (3–4), 711–727. doi:10.1002/nme.4726.
Li, T., 2016. Gradient Damage Modeling of Dynamic Brittle Fracture Ph.D. thesis. Université Paris-Saclay – École Polytechnique.
Li, T., Marigo, J.-J., Guilbaud, D., Potapov, S., 2016. Gradient damage modeling of brittle fracture in an explicit dynamics context. Int. J. Numer. Methods Eng. doi:10.1002/nme.5262.
Lorentz, E., Andrieux, S., 2003. Analysis of non-local models through energetic formulations. Int. J. Solids Struct. 40, 2905–2936.
Marigo, J.-J., Maurini, C., Pham, K., 2016. An overview of the modelling of fracture by gradient damage models. Meccanica 51 (12), 3107–3128. doi:10.1007/s11012-016-0538-4.

Maurini, C., Bourdin, B., Gauthier, G., Lazarus, V., 2013. Crack patterns obtained by unidirectional drying of a colloidal suspension in a capillary tube: experiments and numerical simulations using a two-dimensional variational approach. Int. J. Fract. 184 (1–2), 75–91. doi:10.1007/s10704-013-9824-5.
Mesgarnejad, A., Bourdin, B., Khonsari, M.M., 2015. Validation simulations for the variational approach to fracture. Comp. Methods Appl. Mech. Eng. 290, 420–437.
Miehe, C., Aldakheel, F., Raina, A., 2016. Phase field modeling of ductile fracture at finite strains. a variational gradient-extended plasticity-damage theory. Int. J. Plasticity doi:10.1016/j.ijplas.2016.04.011.
Miehe, C., Hofacker, M., Schänzel, L.-M., Aldakheel, F., 2015. Phase field modeling of fracture in multi-physics problems. Part II. Coupled brittle-to-ductile failure criteria and crack propagation in thermo-elastic-plastic solids. Comp. Meth. Appl. Mech. Eng. 294, 486–522. doi:10.1016/j.cma.2014.11.017.
Mielke, A., 2005. Evolution of rate-indipendent system. In: Dafermos, C., Feireisl, E. (Eds.), Handbook of Differential Equations, Evolutionary Equations, 2. Elsevier, pp. 461–559. 6
Muskhelishvili, N.I., 1977. Some Basic Problems of the Mathematical Theory of Elasticity: Fundamental Equations, Plane Theory of Elasticity, Torsion, and Bending (translated from Russian), 2nd edition Noordhoff International Publishing, Leyden, The Netherlands.
Negri, M., Paolini, M., 2001. Numerical minimization of the Mumford-Shah functional. Calcolo 38 (2), 67–84.
Nguyen, T.T., Yvonnet, J., Bornert, M., Chateau, C., Sab, K., Romani, R., Le Roy, R., 2016. On the choice of parameters in the phase field method for simulating crack initiation with experimental validation. Int. J. Fracture 197 (2), 213–226. doi:10.1007/s10704-016-0082-1.
Ortiz, M., Pandolfi, A., 1999. Finite-deformation irreversible cohesive elements for three-dimensional crack-propagation analysis. Int. J. Num. Meth. Eng. 44, 1267–1282.
Pham, K., Amor, H., Marigo, J.-J., Maurini, C., 2011. Gradient damage models and their use to approximate brittle fracture. Int. J. Damage Mech. 20 (4, SI), 618–652. doi:10.1177/1056789510386852.
Pham, K., Marigo, J.-J., 2010a. Approche variationnelle de l'endommagement: I. Les concepts fondamentaux. The variational approach to damage: I. The foundations. C.R. Mécanique 338 (4), 191–198. doi:10.1016/j.crme.2010.03.009.
Pham, K., Marigo, J.-J., 2010b. Approche variationnelle de l'endommagement: II. Les modèles à gradient. The variational approach to damage: II. The gradient damage models. C.R. Mécanique 338 (4), 199–206. doi:10.1016/j.crme.2010.03.012.
Pham, K., Marigo, J.-J., Maurini, C., 2011. The issues of the uniqueness and the stability of the homogeneous response in uniaxial tests with gradient damage models. J. Mech. Phys. Solids 59 (6), 1163–1190. doi:10.1016/j.jmps.2011.03.010.
Pham, K.H., Ravi-Chandar, K., Landis, C.M., 2017. Experimental validation of a phase-field model for fracture. Int. J. Fract. 205 (1), 83–101. doi:10.1007/s10704-017-0185-3.
Rice, J.R., 1980. The mechanics of earthquake rupture. In: Dziewonski, A.M., Boschi, E. (Eds.), Proc. Int. School of Physics "Enrico Fermi" Physics of the Earth's Interior. North-Holland.
Schmidt, B., Fraternali, F., Ortiz, M., 2009. Eigenfracture: An eigendeformation approach to variational fracture. Multiscale Model. Simul. 7 (3), 1237–1266.
Seweryn, A., 1994. Brittle fracture criterion for structures with sharp notches. Eng. Fract. Mech. 47 (5), 673–681.
Sicsic, P., Marigo, J.-J., 2013. From gradient damage laws to Griffith's theory of crack propagation. J. Elasticity 113 (1), 55–74.
Silling, S.A., 2000. Reformulation of elasticity theory for discontinuities and long-range forces. J. Mech. Phys. Solids 48 (1), 175–209.
Strandberg, M., 2002. Fracture at V-notches with contained plasticity. Eng. Fract. Mech. 69 (3), 403–415.
Wheeler, M.F., Wick, T., Wollner, W., 2014. An augmented-Lagrangian method for the phase-field approach for pressurized fractures. Comp. Methods Appl. Mech. Eng. 271, 69–85.
Wilson, Z.A., Borden, M.J., Landis, C.M., 2013. A phase-field model for fracture in piezoelectric ceramics. Int. J. Fract. 183 (2), 135–153. doi:10.1007/s10704-013-9881-9.
Wilson, Z.A., Landis, C.M., 2016. Phase-field modeling of hydraulic fracture. J. Mech. Phys. Solids 96, 264–290. doi:10.1016/j.jmps.2016.07.019.
Yosibash, Z., Bussiba, A., Gilad, I., 2004. Failure criteria for brittle elastic materials. Int. J. Fract. 125 (3–4), 307–333.
Zhang, X., Vignes, C., Sloan, S.W., Sheng, D., 2017. Numerical evaluation of the phase-field model for brittle fracture with emphasis on the length scale. Comput. Mech. 1–16. doi:10.1007/s00466-017-1373-8.